Inorganic Chemistry

pubs.acs.org/IC Article

Doublet Ground State in a Vanadium(II) Complex: Redox and Coordinative Noninnocence of Tripodal Ligand Architecture

Justin P. Joyce,[‖] Romeo I. Portillo,[‖] Anthony K. Rappé,* and Matthew P. Shores*

Cite This: *Inorg. Chem.* 2022, 61, 6376–6391 Read Online

ACCESS | Metrics & More | Article Recommendations | Supporting Information

ABSTRACT: We report on the geometric and electronic structures of a series of $V^{2+/3+}$ tren-bridged iminopyridine complexes [tren = tris(2-aminoethyl)amine] that enable the observation of an unexpected doublet ground state for a nominally $3d^3$ species. Tren undergoes condensation reactions with picolinaldehyde or methyl-6-formylnictonate to form the respective tripodal ligand sets of $(py)_3$tren and $(5\text{-}CO_2Mepy)_3$tren. The $(py)_3$tren ligand is coordinated to V^{2+} and V^{3+} metal centers to form complex salts $[\mathbf{1\text{-}H}](OTf)_2$ and $[\mathbf{1\text{-}H}](OTf)_3$, respectively ($OTf^- = CF_3SO_3^-$). For $[\mathbf{1\text{-}H}]^{2+}$, strong metal−ligand π-covalency with respect to the V^{2+} ($3d^3$) and iminopyridine ligands weakens its interelectronic repulsion. For $[\mathbf{1\text{-}H}]^{3+}$, the bridgehead nitrogen of the tren scaffold forms a seventh coordinate covalent bond with a V^{3+} ($3d^2$) metal center. The coordination of $(5\text{-}CO_2Mepy)_3$tren to a V^{2+} metal center results in the redox noninnocent and heptacoordinate compound $[\mathbf{1\text{-}CO_2Me}](OTf)_2$ with a doublet ($S = {}^1/_2$) ground state that we support with magnetic susceptibility and spectroscopy measurements. The complexes are uniformly characterized experimentally with single-crystal X-ray diffraction, electronic absorbance, and electrochemistry, and electronic structures are corroborated by computational techniques. We present a new computational procedure that we term the spin-optimized approximate pair (SOAP) method that enables the visualization and quantification of electron−electron interactions.

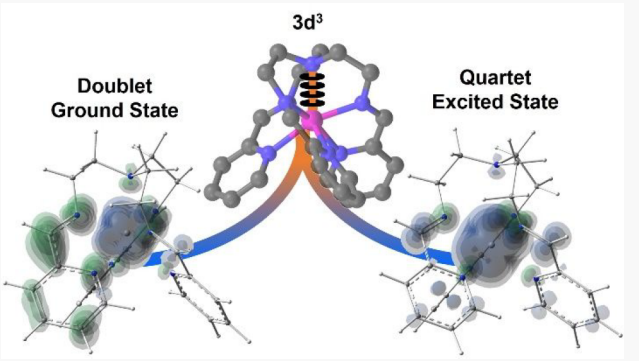

INTRODUCTION

An increasing amount of effort has been directed toward the integration of first-row transition metal ions into photocatalytic processes that are traditionally associated with precious congeners.[1−10] Earth-abundant coordination complexes strain confinement by the chemical properties of their noble metal analogues. Attributable to the weakened covalency of their metal−ligand bonds, 3d complexes possess many low-lying excited states that can have distinct electronic spin multiplicities. While these near-degenerate states are advantageous with respect to molecular magnetism,[11−14] they convolute direct mechanistic pathways for catalytic transformations.[15−24] Octahedral Cr^{3+} polypyridyl complexes have been demonstrated to facilitate photocatalytic and photoredox processes.[25−29] The low-lying ^2E excited state of d^3 complexes is classified as a spin-flip transition whose energy is approximately independent of ligand field strength but proportional to the interelectronic repulsion between its metal-centered electrons.[30,31] Weakening the interelectronic repulsion, via metal−ligand covalency, has been recently demonstrated by Wenger and Piguet[32] and Heinze[33] as a robust design principle to impact the energy of the ^2E state of a Cr^{3+} complex. The ability to modulate the energies of states of different multiplicities in first-row transition metals impacts their ability to perform catalysis.[34]

Despite potential environmental advantages, photocatalysis has not been extended to the isoelectronic (d^3) V^{2+}analogue due to greater π-bonding with its polypyridyl ligand set that results in a low-lying doublet state of both metal-centered (MC) and metal-to-ligand charge transfer (MLCT) character.[35−37] The resonance of this ^{2}MC/^{2}MLCT state of V^{2+} polypyridyls significantly stabilizes its doublet excited state. We report the observation of a doublet ground state in a V^{2+} tren-iminopyridine system whose ligand environment stabilizes the doublet state through several dramatic changes in the covalency of the system that are illustrated in Figure 1 and detailed herein. The characterization of the doublet state of $3d^3$ complexes has only previously been accessible through transient spectroscopic and computational techniques.[38−41]

Herein, we combine spectroscopic and theoretical methods to address the unique electronic and geometric structures of our vanadium tripodal complexes. We present a model that

Received: November 1, 2021
Published: April 15, 2022

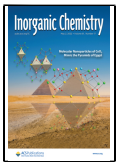

https://doi.org/10.1021/acs.inorgchem.1c03418
Inorg. Chem. 2022, 61, 6376−6391

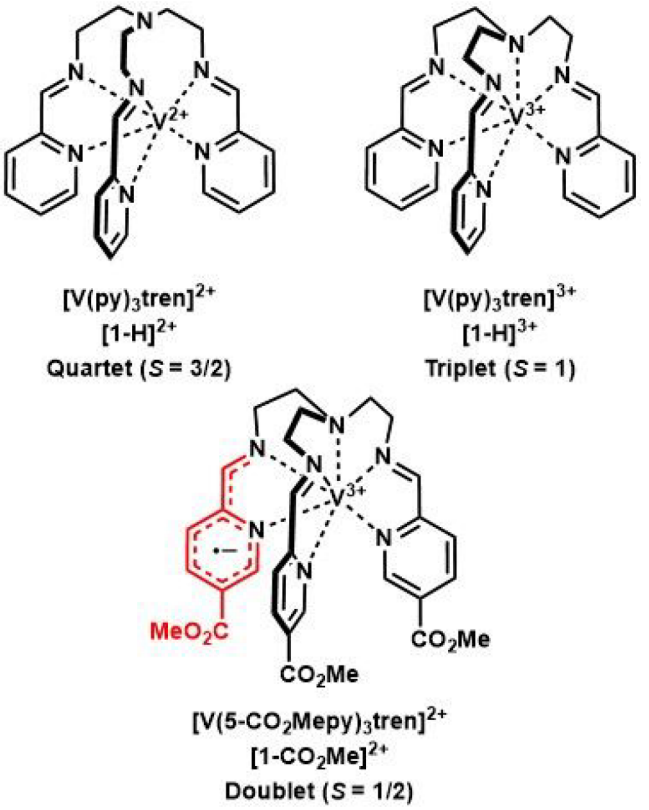

Figure 1. Illustrated geometric structures, chosen notation and abbreviations, and spin multiplicities of the three vanadium tren-iminopyridine complexes detailed in our report. Tren refers to tris(2-aminoethyl)amine, whose C_3-symmetric arrangement of primary amines undergoes condensation reactions with picolinaldehyde or methyl-6-formylnicotinate to form the respective tripodal ligand set of $(py)_3$tren and $(5\text{-}CO_2Mepy)_3$tren. The $(py)_3$tren ligand set is coordinated to V^{2+} and V^{3+} metal centers to form complexes $[\mathbf{1}\text{-}\mathbf{H}]^{2+}$ and $[\mathbf{1}\text{-}\mathbf{H}]^{3+}$, respectively. The coordination of $(5\text{-}CO_2Mepy)_3$tren to a V^{2+} metal center results in redox noninnocent complex $[\mathbf{1}\text{-}\mathbf{CO_2Me}]^{2+}$, whose reduced iminopyridine group is colored red.

provides visual and quantitative insight into the discrete electron−electron interactions of open-shell systems. Our spin-optimized approximate pair (SOAP) method cultivates an understanding through generation of three-dimensional (3D) graphics of the structural properties that impact the energy of spin-flip excited states. This has been a recent focus of d^2 and d^3 transition metal systems.[6,42−46] Our approach is a natural extension of the general valence bond (GVB) treatment of small open-shell molecules developed by Goddard and Bobrowicz[47−49] and finding further articulation with research from Dunning and Cooper.[50−53] Our SOAP method can be extended to systems irrespective of the total number of unpaired electrons or competing magnetic interactions, to provide new insights into the root causes of ferro- and antiferromagnetic coupling.

RESULTS AND DISCUSSION

V^{2+}-Iminopyridine: Metal−Ligand and π-Covalency. First, we detail the strong metal−ligand π-covalency between the V^{2+} metal center and the iminopyridine ligand set in complex $[\mathbf{1}\text{-}\mathbf{H}]^{2+}$, the compound notation being detailed in the legend of Figure 1. The subsequent reduction in the interelectronic repulsion between the unpaired electrons on the paramagnetic metal center decreases the gap between the quartet ground and doublet excited states. This is manifested as a 0.09 eV reduction in exchange with respect to its bipyridyl analogue $[V(bpy)_3]^{2+}$ (bpy = 2,2′-dipyiryl), which helps facilitate the doublet ground state that we will detail with respect to $[\mathbf{1}\text{-}\mathbf{CO_2Me}]^{2+}$ below.

Diffraction quality single crystals of $[\mathbf{1}\text{-}\mathbf{H}]^{2+}$ are obtained by the slow diffusion of diethyl ether into acetonitrile, and the structure is shown in Figure 2. Structures of $[\mathbf{1}\text{-}\mathbf{H}]^{3+}$ and $[\mathbf{1}\text{-}\mathbf{CO_2Me}]^{2+}$ are also included in Figure 2. While the tren-iminopyridine ligand environment is known for third-row transition metal complexes, these are the first structures reported for $V^{2+/3+}$.[54] Key bond distances and structural parameters are listed in Table 1. The imine and pyridine donor atoms of $[\mathbf{1}\text{-}\mathbf{H}]^{2+}$ possess nearly equivalent bond lengths. The structure displays a $V^{2+}-N_{bridge}$ distance that is intermediate between a coordinate covalent bond and a noncovalent interaction, when scaled with respect to the sum of their covalent radii ($R\sum cov^{-1}$) that is a factor of 1.41.[55]

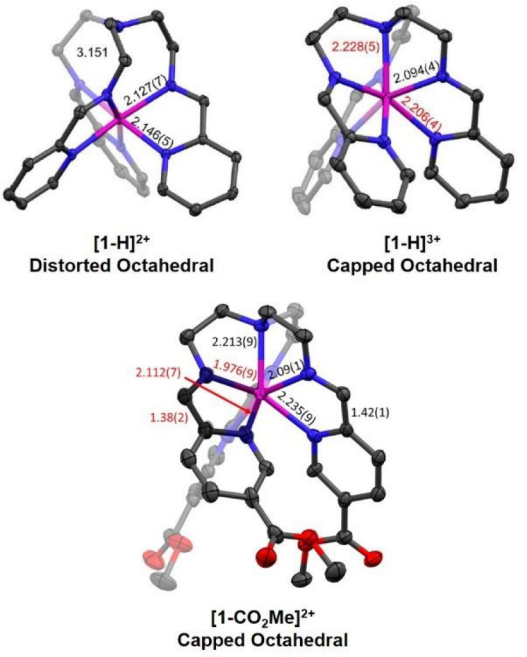

Figure 2. Experimental molecular structures of $[\mathbf{1}\text{-}\mathbf{H}]^{2+}$, $[\mathbf{1}\text{-}\mathbf{H}]^{3+}$, and $[\mathbf{1}\text{-}\mathbf{CO_2Me}]^{2+}$, as determined by X-ray crystallography, where hydrogen atoms, anions, and co-crystallized solvent molecules have been omitted for the sake of clarity. The notation of these complexes is detailed in the legend of Figure 1. Thermal ellipsoids are set to 40%. Assigned coordination geometries, pertinent bond distances, and interatomic separations (in angstroms) are provided. Pink, blue, black, and red ellipsoids represent vanadium, nitrogen, carbon, and oxygen, respectively.

The separation between the bridgehead nitrogen (N_{bridge}) of the tren scaffold and the transition metal center is established to be dependent on the oxidation and spin state.[57−62] We have previously reported that the N_{bridge} conformation impacts the local electronic structure of its transition metal center with respect to the photophysics of Cr^{3+} and the molecular magnetism of Co^{2+} complexes.[63,64] The value for the continuous shape measure (CShM) of a six-coordinate octahedral environment is termed S(OC-6), where a greater

https://doi.org/10.1021/acs.inorgchem.1c03418
Inorg. Chem. 2022, 61, 6376−6391

Table 1. Key Metric Parameters of Detailed Vanadium Complexes[a]

	$[1\text{-H}]^{2+}$	$[1\text{-H}]^{3+}$	$[1\text{-CO}_2\text{Me}]^{2+}$
$V-N_{bridge}$ (Å)	3.151	2.228(5)	2.213(9)
$V-N_{imine}$ (Å)	2.127(7)	2.094(4)	2.10(1)
$V-(N_{imine})^-$ (Å)			1.976(9)
$V-N_{pyridine}$ (Å)	2.146(5)	2.206(4)	2.20(4)
$V-(N_{pyridine})^-$ (Å)			2.112(7)
S(OC-6) (unitless)	1.480	2.503	2.521
S(COC-7) (unitless)	3.055	0.792	0.943

[a]Bond lengths are reported in angstroms, and S(OC-6) and S(COC-7) refer to the continuous shape measure (CShM) values for octahedral and capped octahedral coordination geometries, respectively.[56]

value indicates greater distortion from its ideal shape that is determined with SHAPE version 2.2.[56] The CShM values do not possess units for the coordination geometries considered herein because it is referenced to an ideal shape. The S(OC-6) of $[1\text{-H}]^{2+}$ is 1.480, and its primary coordination sphere is best classified as distorted octahedral. This is increased with respect to our previous analysis of the polypyridyl analogue $[V(bpy)_3]^{2+}$ whose density functional theory (DFT)-optimized structure has an S(OC-6) of 1.27.[37] This suggests greater metal−ligand π-covalency for the iminopyridine coordination environment because of the loss of degeneracy in the t_{2g} orbitals as the complex is distorted toward a trigonal, C_3-symmetric environment, where $t_{2g} \rightarrow e + a^*$.

The electronic absorbance spectra of $[1\text{-H}]^{2+}$ and its polypyridyl analogue, $[V(bpy)_3](OTf)_2$ (OTf^- = trifluoromethylsulfonate), are included in Figure 3. The absorbance

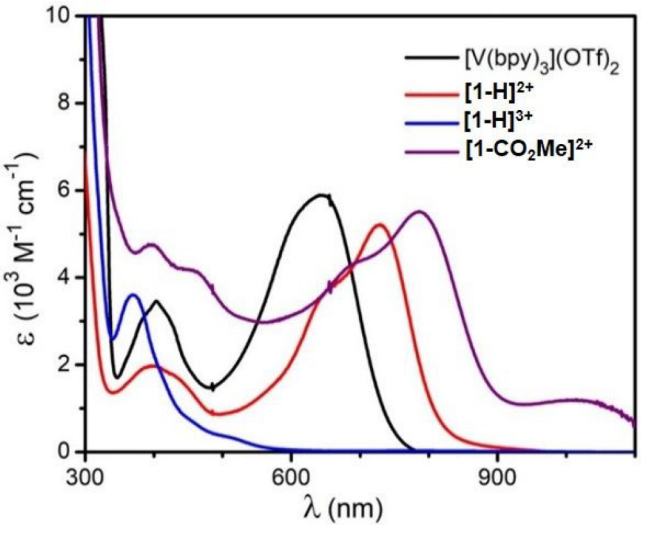

Figure 3. Electronic absorption spectra of $[1\text{-H}]^{2+}$, $[1\text{-H}]^{3+}$, and $[1\text{-CO}_2\text{Me}]^{2+}$, recorded in acetonitrile. The corresponding spectrum of $[V(bpy)_3](OTf)_2$[35] is provided as a reference to the impact of the iminopyridine ligand environment.

data of $[1\text{-H}]^{3+}$ and $[1\text{-CO}_2\text{Me}]^{2+}$ are also included in Figure 3 and are detailed further below. $[1\text{-H}]^{2+}$ exhibits a broad electronic absorbance at approximately 750 nm that we assign as a metal-to-ligand charge transfer (MLCT). This is consistent with the transition's large molar absorptivity (ε) and the small ionization potential of a V^{2+} metal center.[36,65] The MLCT is red-shifted by 0.28 eV with respect to the polypyridyl analogue, which we attribute to the higher electron affinity of the iminopyridine with respect to the bipyridine ligand set. Our assignment is further corroborated by time-dependent density functional theory (TD-DFT),[66] whose natural transition spin density plots ($NT\rho^{\alpha,\beta}$)[37] are included in Table S4 and Figure S13.

The computed electronic ground state of $[1\text{-H}]^{2+}$ is a quartet ($S = {}^3/_2$), the $^4A_2$ state common for d^3 systems in a nominally octahedral coordination environment.[31] The lowest-lying doublet state is ^2E that our detailed multideterminant DFT computation assigns as 0.96 eV above the ground state for $[1\text{-H}]^{2+}$.[67] We note that the A_2 and E term symbols are preserved for the C_3-symmetric environment of the tripodal ligand architecture in our detailed V^{2+} complexes. Comparatively, we have reported that $[V(bpy)_3]^{2+}$ should have a ^2E excited state of 1.10 eV.[37] We reference the spin density of ^2E of $[1\text{-H}]^{2+}$ to its $^4A_2$ ground state in our relative spin density plot ($\Delta\rho^{\alpha,\beta}$) in Figure 4.[37] While the ^2E state is traditionally

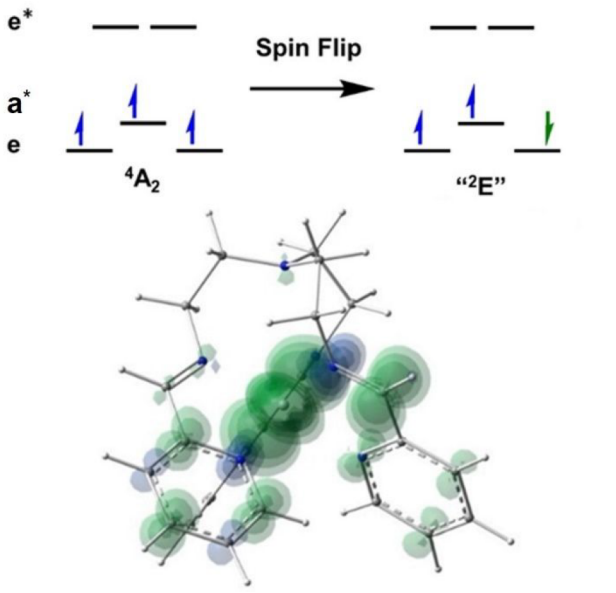

Figure 4. Electronic configuration of the lowest-lying quartet and doublet states for C_3-symmetric d^3 complexes, where the quotation marks denote a single-determinant description in the context of DFT (top). The a* orbital is destabilized by 0.22 eV with respect to the lowest-lying e orbitals, as determined from the orbital energies of the APFD-calculated quartet state. APFD spin density of the lowest-lying doublet state of the vanadium complex of $[1\text{-H}]^{2+}$ (bottom), referenced against its lowest-lying quartet state for our relative spin density ($\Delta\rho^{\alpha,\beta}$) plot. Green denotes a loss of α and an increase of β electron spin density in the lowest-lying quartet and doublet states, respectively. The contours are shown at 0.003, 0.006, and 0.012 electron $bohr^{-2}$.

characterized as a metal-centered spin flip, the $\Delta\rho^{\alpha,\beta}$ plot shows that it is significantly delocalized onto the iminopyridine ligand set for $[1\text{-H}]^{2+}$.

The impact of metal−ligand covalency on the ^2E excited state energy is that it weakens the interelectronic repulsion between the singly occupied metal-centered orbitals.[68−70] The unpaired electrons of the $^4A_2$ state of $[1\text{-H}]^{2+}$ occupy orbitals that are orthogonal and nearly degenerate so that Hund's first rule applies.[71−73] The basis for a quartet ground state is the three favorable exchange interactions between electrons of parallel spin (K_{ab}), detailed in section S7.1 of the Supporting

https://doi.org/10.1021/acs.inorgchem.1c03418
Inorg. Chem. 2022, 61, 6376−6391

Information.[74−76] The discussion in section S7.1 similarly addresses the Jahn−Teller distortion of the ^{2}E state and the difficulty of its multideterminant character with DFT methods. The Pauli exclusion principle prohibits electrons of the same spin from occupying the same location, thus weakening a system's interelectronic repulsion via electron correlation. This can be termed Fermi correlation and is addressed in Hartree−Fock theory with respect to the antisymmetry of the Slater determinant.[77] If the unpaired electrons are restricted by symmetry from bonding, then exchange remains as the sole resource of stabilization.

Introducing the Spin-Optimized Approximate Pair (SOAP) Method. To visualize the impact of exchange on state energy differences, we present a model that provides 3D graphical representations of electron−electron interactions that we term the spin-optimized approximate pair (SOAP) method. While our current focus is the exchange interactions, our procedure similarly extends to Coulombic and more complex interelectronic interactions that are detailed in section S6. K_{ab} possesses the form of an electrostatic potential that is detailed in eq 1. While the Coulombic interaction between a pair of electrons occurs with their physically measurable charge densities, K_{ab} is the electrostatic repulsion that occurs in the unmeasurable regions where the orbitals overlap. *Exchange is a classical interaction with a quantum mechanical origin.* Dougherty has previously referred to areas of interference between orbitals as the overlap functional (f_{ab}) that is illustrated in eq 2.[78]

$$K_{ab} = \int\int \frac{\phi_a(1)\phi_b(1)\phi_a(2)\phi_b(2)}{r_{12}}\, dr_1\, dr_2 \quad (1)$$

$$K_{ab} = \int\int \frac{f_{ab}^{\,2}}{r_{12}}\, dr_1\, dr_2 \quad (2)$$

In Figure 5, we plot a representative exchange interaction between a pair of singly occupied metal-centered orbitals of $[\mathbf{1\text{-}H}]^{2+}$ as an electrostatic potential overlaid on the surface density of the respective f_{ab}.[79] The exchange interaction is dominantly metal-centered because there is little overlap between the portions of the respective orbitals that are delocalized onto the ligand set. Here, blue and red represent areas in which the interference between the singly occupied orbitals displays positive and negative coherence, respectively. Because the current orbitals are orthogonal, the amount of in-phase and out-of-phase overlap will be equal.

Overall, K_{ab} is a repulsive interaction whose energetic impact on the system depends on the orientation of the electron spins that is favorable for aligned spins. Metal−ligand π-covalency delocalizes the singly occupied V^{2+} orbitals onto the ligand, thus reducing the f_{ab} overlap functional and the magnitude of their exchange interactions. We note that K_{ab} can be similarly plotted as a surface density, which describes the integrand in eq 1 or 2, providing a quantitative numerical value that is provided in Figure 5. Our SOAP method provides both visual and nearly quantitative values for discrete electron−electron interactions. This is distinct from the information provided in Figure 4 in that it illustrates the magnitude of the spin-flip excited state energy and suggests that exchange interactions can be modulated via established synthetic principles for metal−ligand covalency. We also note that the spin densities of antiferromagnetically coupled systems are nonphysical and cannot be related, without projection methods, to experimental

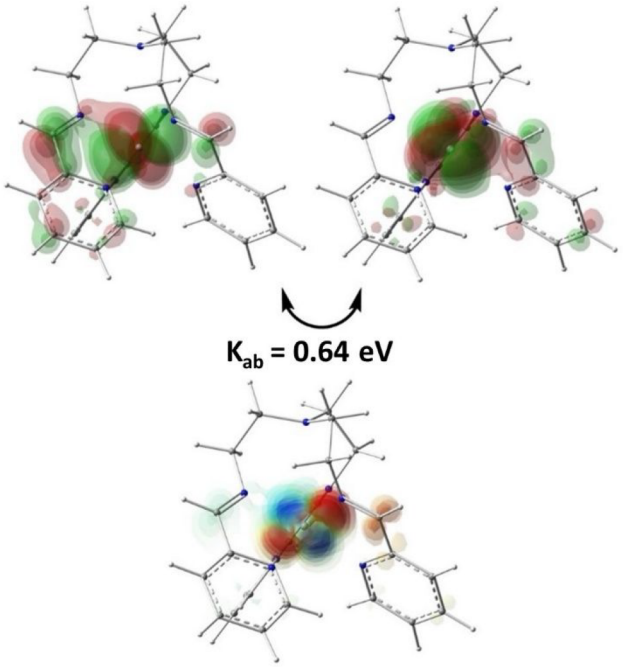

Figure 5. Two lowest-lying singly occupied molecular orbitals of the vanadium complex $[\mathbf{1\text{-}H}]^{2+}$ that possess e-symmetry with respect to the complex's C_3 coordination environment (top). The orbitals are obtained from the corresponding CASSCF(3,8) wave function. The contours are shown from 0.025 to 0.045 in increments of 0.01 electron bohr^{-2}. Exchange potential and integrand associated with K_{ab} obtained with our SOAP method (bottom). Blue and red denote an exchange potential that results from positive and negative overlap, respectively, between the two lowest-lying singly occupied molecular orbitals shown in the top panel. The f_{ab} contours are shown for 0.001, 0.002, and 0.004 electron bohr^{-2}. The colors range from −0.235 (red) to 0.235 (blue) hartree bohr^{-2}.

results that include electron paramagnetic resonance (EPR) spectroscopy.[80,81] We will detail an antiferromagnetically coupled system with respect to the electronic structure of $[\mathbf{1\text{-}CO_2Me}]^{2+}$ provided below. The orbitals for our SOAP method are generated from the natural orbitals of the complete active space self-consistent field (CASSCF) wave function in which the active space is defined as the metal-centered 3d orbitals and ligand-centered π^* orbitals.[82] The excited state energies of both quartet and doublet multiplicities are further refined with the *n*-electron valence state perturbation theory (NEVPT2) that accounts for dynamic correlation.[83−85] Our multireference calculations were performed with the ORCA 4.1 electronic structure software package.[86]

Heptacoordination with the Tren Scaffold. Oxidation of $[\mathbf{1\text{-}H}]^{2+}$ with silver triflate (AgOTf) produces the V^{3+} complex $[\mathbf{1\text{-}H}]^{3+}$. The structure (Figure 2) features a seventh coordinate covalent bond, now involving the tertiary amine (N_{bridge}) of the tren backbone. Relative to that of $[\mathbf{1\text{-}H}]^{2+}$, the V−$N_{bridge}$ distance for $[\mathbf{1\text{-}H}]^{3+}$ contracts by 0.92 Å to 2.228(5) Å, which is smaller than the sum of their covalent radii [$R\sum$cov^{-1} = 0.995(2)].[55] As shown in Table 1, whereas $[\mathbf{1\text{-}H}]^{2+}$ shows relatively equal V−N distances, for $[\mathbf{1\text{-}H}]^{3+}$, significant deviation is apparent in the metal−ligand bond lengths of the imine and pyridine donor atoms.

Complex $[\mathbf{1\text{-}H}]^{3+}$ displays the shortest metal−bridgehead nitrogen contact among the reported tren systems. The structure of $[\mathbf{1\text{-}H}]^{3+}$ is well-defined by the CShM for a capped

https://doi.org/10.1021/acs.inorgchem.1c03418
Inorg. Chem. 2022, 61, 6376−6391

octahedral geometry [S(COC-7) = 0.791], an arrangement that is favored in tren-containing systems but relatively anomalous in the full catalogue of heptacoordinate complexes.[62] A greater value of S(COC-7) indicates greater distortion from the seven (hepta)-coordinate geometry of a reference capped octahedral coordination environment. While analogous Mn^{2+} complex geometries have been assigned as capped octahedral, the separation from N_{bridge} is primarily an impact of crystal packing forces.[61,87,88] In contrast, as we will outline below, heptacoordination is a source of stability for the d^2 electronic configuration of V^{3+}, which will help facilitate the doublet ground state we observe for $[\mathbf{1\text{-}CO_2Me}]^{2+}$.

Heptacoordination can be understood in terms of the hybridization between the metal d orbitals. Independent of metal identity, the σ-bonding abilities of the five d orbitals are inequivalent, and greatest for the d_{z^2} orbital.[89,90] In octahedral symmetry, the solitary d_{z^2} orbital points along a metal−ligand bond axis. Interestingly, the symmetric linear combination of the π-symmetric octahedral t_{2g} orbitals (d_{xz}, d_{yz}, and d_{xy}) forms a hybridized orbital of pure d orbital and σ symmetry character along a 3-fold octahedral axis with a bond strength equivalent to that of the d_{z^2} orbital. We refer to this orbital as d_σ, and a plot of it is shown in Figure 6.[91,92] We note that our current

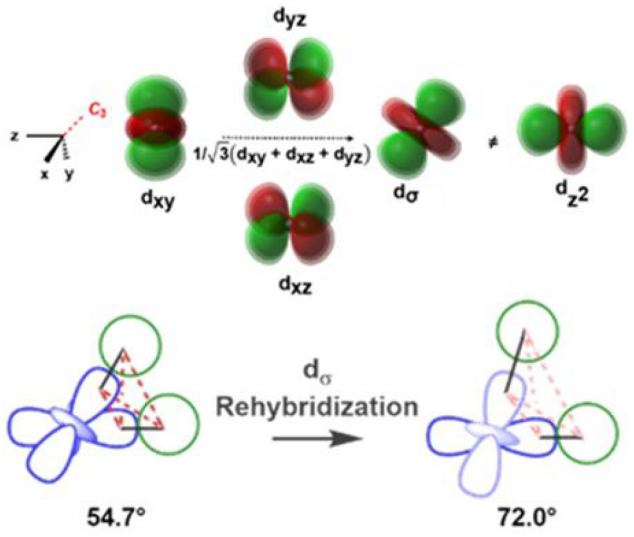

Figure 6. Symmetric hybridization among the d_{xy}, d_{xz}, and d_{yz} orbitals that constitute the t_{2g} set with respect to an octahedral coordination environment (top). This generates a d_σ orbital that is equivalent to the d_{z^2} orbital but rotated 54.7° along its nodal zone. The contours are shown from 0.025 to 0.045 in increments of 0.01 electron $bohr^{-2}$. Rehybridization of the d_σ orbital from the ideal bond angle of 54.7° to the experimental bond angle of 72.0° to remove its angular overlap with the d_{z^2} orbital (bottom). This hybridization results in the orbital character of a capped octahedral, C_3-symmetric coordination environment detailed in Figure 2.

model is distinct from a group theory approach that assigns the d orbital oriented along the C_3-symmetry axis as d_{z^2} that has been previously detailed by McGarvey and Telser[93] and Atanasov and Neese.[14] The C_3-symmetric "a" orbital does not interfere with the "octahedral" orbitals of e_g^* symmetry that is the basis of the following discussion.

We can consider the strength of the hypervalent metal−ligand bond involving d_σ using principles of orbital orthogonality that stem from the classic work of Pauling[89] and Hultgren[90] that were later refined by Landis.[94−97] Irrespective of coordination number, we refer to a transition metal center as hypervalent if it possesses an orbital of σ-bonding character that is equivalent to its d_{z^2} orbital. Equation 3 details the angular overlap (S_{12}) between the d_σ and d_{z^2} orbital based on the angle between the seventh ligand and the adjacent metal−ligand bond (θ). At an angle of 54.7°, the orbitals have an angular overlap of 0 so that they are orthogonal. The directional character of this d_σ orbital is equivalent to that of the d_{z^2} orbital that is related to its σ-bond strength with an interacting ligand. The orbital energy of this d_σ orbital is +0.60Δ with respect to the ligand field splitting of its corresponding octahedral coordination environment.[98] Due to interelectronic repulsion between the metal−ligand σ-bonds, the angle expands to approximately 72° as reported by Hoffmann, Muetterties, and co-workers and illustrated in Figure 6.[99] This is consistent with the structure of $[\mathbf{1\text{-}H}]^{3+}$ that displays an average $\angle N_{bridge}\text{−}V\text{−}N_{imine}$ bond angle of 71.5(3)° corresponding to an S_{12} value of 0.35 with respect to the d_σ and d_{z^2} orbitals. This posits that the strength of the hypervalent $V\text{−}N_{bridge}$ bond of $[\mathbf{1\text{-}H}]^{3+}$ is a factor of 0.65 ($1 - S_{12}$) that is equal to +0.25Δ with respect to the remaining metal−ligand σ-bonds of the octahedral coordination environment.

$$S_{12} = \left| \frac{3\cos^2\theta - 1}{4} \right| \tag{3}$$

The ligand field transition energies are centered at 774 and 506 nm, highlighted in Figure S6, and illustrated with our $NT\rho^{\alpha,\beta}$ plots in Figure 7. These ligand field transitions are descriptive of the C_3 symmetry of the tripodal scaffold that reduces the 3-fold degeneracy of $t_{2g} \rightarrow e + a^*$. This reduction in symmetry shifts the reference energy (barycenter) of the complex, stabilizing the lower- and upper-lying e orbitals. The difference in energy between the d_σ (a^*) and lowest-lying e orbitals relative to the octahedral ligand field splitting (Δ) is equal to the deviation in the angular overlap from unity that we term Δ_3 in eq 4.

$$1 - S_{12} = \left(\frac{a^* \leftarrow e}{e^* \leftarrow e} \right) = \Delta_3 \tag{4}$$

Equation 5 provides the change in ligand field stabilization energy (ΔLFSE) associated with a d^n metal center adopting a capped octahedral geometry with respect to the corresponding octahedral complex. The experimental bond angle for $[\mathbf{1\text{-}H}]^{3+}$ of 72° suggests that heptacoordination stabilizes the complex by −0.26Δ. This converts to a hypervalent bond strength of 14.8 kcal mol^{-1} if we assume that contraction of the bridgehead nitrogen strictly impacts the energy of the a^* orbital. The experimental ligand field transition of $a^* \leftarrow e$ suggests that coordination of the bridgehead nitrogen stabilizes $[\mathbf{1\text{-}H}]^{3+}$ by an identical value of 14.8 kcal mol^{-1}, which validates our current structural model. Comparatively, a capped octahedral geometry is not anticipated for $[\mathbf{1\text{-}H}]^{2+}$ because the d_σ orbital is populated, heptacoordination destabilizing the complex by +0.26Δ, which is consistent with its experimental $V\text{−}N_{bridge}$ separation shown in Figure 2.

$$\Delta\text{LFSE}(\Delta) = 2\Delta_3[4N(a^*) - N(e^*) - N(e)] \tag{5}$$

Electrochemical experiments further support stabilization from oxidation-activated hypervalency. The cyclic voltammogram of $[\mathbf{1\text{-}H}]^{2+}$ shown in Figure 8 displays a reversible 3+/2+ oxidation at −0.51 V versus Fc^+/Fc^0 in CH_3CN, along with

https://doi.org/10.1021/acs.inorgchem.1c03418
Inorg. Chem. 2022, 61, 6376−6391

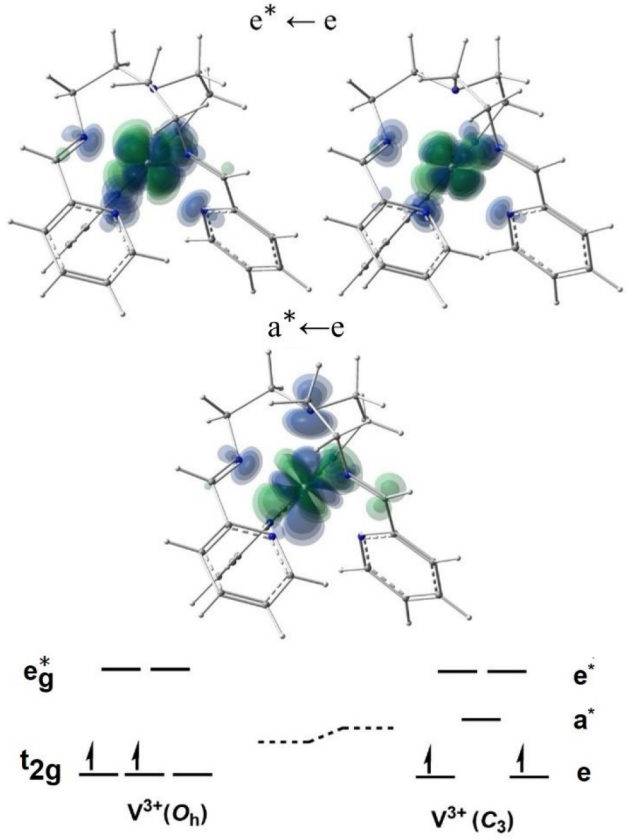

Figure 7. Natural transition spin density ($NT\rho^{\alpha,\beta}$) plots of the ligand field transitions of the vanadium complex of $[\mathbf{1\text{-}H}]^{3+}$ that illustrate the loss of degeneracy associated with heptacoordination to the tren scaffold (top). The contours are shown for 0.003, 0.006, and 0.012 electron bohr^{-2}. Orbital energy diagrams of an ideal hexacoordinate, octahedral, and heptacoordinate, capped-octahedral, V^{3+} (d^2) complex (bottom). The shift in the barycenter (dashed lines) between the octahedral and capped octahedral coordination geometry is shown.

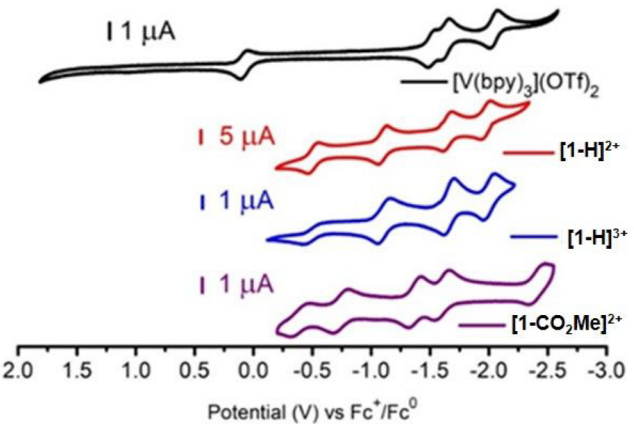

Figure 8. Cyclic voltammograms (0.1 V/s) of the cathodic reduction potentials for $[\mathbf{1\text{-}H}]^{2+}$, $[\mathbf{1\text{-}H}]^{3+}$, $[\mathbf{1\text{-}CO_2Me}]^{2+}$, and $[V(bpy)_3](OTf)_2$.[35] The experiments were performed in 0.1 M Bu_4NPF_6 and CH_3CN.

ligand reductions at −1.09, −1.64, and −1.98 V versus Fc^+/Fc^0. The corresponding V^{2+} bipyridine complex exhibits an $E_{1/2}(3+/2+)$ of 0.08 V, which suggests the tren scaffold stabilizes the V^{3+} oxidation state by 0.59 eV (13.6 kcal mol^{-1}), in agreement with the ΔLFSE values calculated above. Compound $[\mathbf{1\text{-}H}]^{3+}$ displays identical redox properties except that the 3+/2+ couple lacks reversibility. It is interesting to note that the same trend in the electrochemical reversibility of the $E_{1/2}(3+/2+)$ value based on coordination geometry has been previously reported in characterizing spin-labile Fe^{2+} tren-iminopyridine complexes.[100,101] We report a Randles−Sevcik analysis on the 3+/2+ oxidation of $[\mathbf{1\text{-}H}]^{3+}$ in section S2.1 that determines a linear relationship between the total current with respect to the square root of the electrochemical scan rate, $v^{1/2}$. The linear dependence from the Randles−Sevcik analysis of the reduction with respect to the oxidation of the $E_{1/2}(3+/2+)$ couple is 3 times greater. This could suggest that the electrochemical scan rate is on the order of the kinetics of the breaking of the seventh coordinate covalent bond associated with the reduction of complex $[\mathbf{1\text{-}H}]^{3+}$ to $[\mathbf{1\text{-}H}]^{2+}$. The cyclic voltammogram of $[\mathbf{1\text{-}CO_2Me}]^{2+}$ is included in Figure 8 and detailed below.

For the vanadium complexes reported herein, heptacoordination is a redox-mediated process. The conversion between OC-6 and COC-7 has not been previously reported. While spin-labile Fe^{2+} complexes will exhibit a contraction of the tren scaffold when undergoing a low- to high-spin transition, the $Fe-N_{bridge}$ separation does not approach the sum of their covalent radii.[60,61] Halcrow has previously reported that spin crossover is inhibited in these complexes by deviations in the $Fe^{2+}-N_{bridge}$ separation that exceed 0.5 Å upon comparison of low- and high-spin states.[102] Similar to the discussion of Mn^{2+} presented above, the equilibrium position of the N_{bridge} of the tren scaffold of high-spin Fe^{2+} complexes is principally an impact of crystal packing forces.

Doublet Ground State in 1-CO_2Me. Lastly, we detail the roles that heptacoordination and redox noninnocence play in the formation of an unexpected doublet ground state for $[\mathbf{1\text{-}CO_2Me}]^{2+}$. For comparison with previously reported tren structures,[87] we installed an ester substituent that is located *meta* and *para* with respect to the pyridine and imine N donor atoms, respectively. The isovalent Cr^{2+} complex displayed redox noninnocence with an iminopyridine moiety that is descriptive of its triplet ground state.[103] We would anticipate this behavior to be more accessible for V^{2+} systems because their ionization potential (29.31 eV) is smaller than that of Cr^{2+} (30.96 eV). In addition, heptacoordination restores some of the loss of LFSE associated with removing an electron from a t_{2g} orbital from an octahedral V^{2+} complex that is not accessible to Cr^{2+} because its d_σ orbital would be singly occupied.

In agreement with the crystal structure of $[\mathbf{1\text{-}H}]^{3+}$, $[\mathbf{1\text{-}CO_2Me}]^{2+}$ displays structural properties that are consistent with a V^{3+} species, rather than a V^{2+}, oxidation state (Table 1). The $V-N_{bridge}$ separation of $[\mathbf{1\text{-}CO_2Me}]^{2+}$ is 2.213(9) Å, equal to 0.988(4) $R\sum cov^{-1}$. The CShM classifies $[\mathbf{1\text{-}CO_2Me}]^{2+}$ as a capped octahedral geometry in which S(COC-7) is equal to 0.908 that is more distorted than $[\mathbf{1\text{-}H}]^{3+}$. The anticipated C_3 symmetry is not observed for $[\mathbf{1\text{-}CO_2Me}]^{2+}$, as the $V-N_{imine}$ and $V-N_{pyridine}$ bond lengths of the trigonal ligand set are inequivalent. Two of the coordinated groups have average $V-N_{imine}$ and $V-N_{pyridine}$ bond lengths of 2.10(1) and 2.20(4) Å, respectively, that are consistent with a V^{3+} metal center. In those two iminopyridine ligand arms, the $C_{imine}-C_{pyridine}$ bond distance is 1.42(1) Å. The $C_{imine}-C_{pyridine}$ bond length of the remaining iminopyridine group contracts to 1.38(2) Å, suggestive of the partial double-bond character that accompanies a one-electron reduction.[104] The N donor atoms display

https://doi.org/10.1021/acs.inorgchem.1c03418
Inorg. Chem. 2022, 61, 6376−6391

contracted V−N_{imine} and V−$N_{pyridine}$ bond lengths of 1.976(9) and 2.112(7) Å, respectively, which can be attributed to greater Coulombic attraction between the cationic transition metal center and anionic ligand radical. The ester substituents are in the plane of the iminopyridine groups, and their dihedral angle (φ) is 14(4)°, whose π^* orbitals of the ester functional group are conjugated with that of the aromatic ligand set.

Collectively, the structural features of $[\mathbf{1\text{-}CO_2Me}]^{2+}$ are consistent with a V^{3+} metal center resulting from redox noninnocence of an iminopyridine moiety. Literature precedent suggests that the spin centers should be antiferromagnetically coupled, resulting in a doublet ground state.[105,106] To support this spin assignment, we analyzed the product of the magnetic susceptibility (χ_M) and temperature (T) of $[\mathbf{1\text{-}CO_2Me}]^{2+}$ as a function of temperature in Figure 9. At low

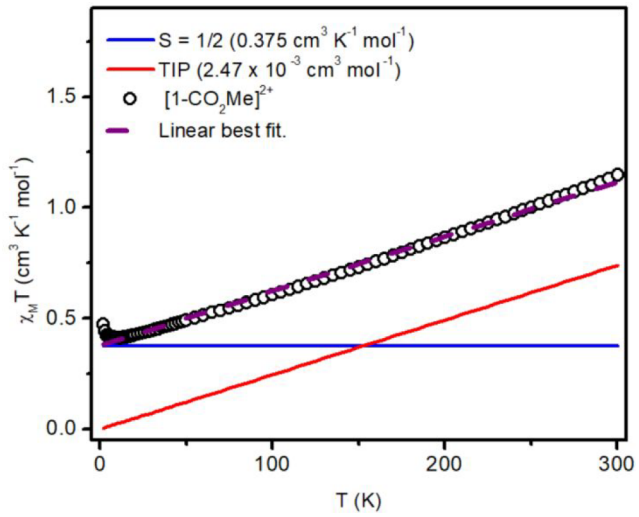

Figure 9. Temperature dependence of the magnetic susceptibility for a powdered sample of $[\mathbf{1\text{-}CO_2Me}]^{2+}$, collected with a 1 kOe measurement field. The linear best fit of the experimental data is $\chi_M T = 0.377 + (2.47 \times 10^{-3})T$ ($R^2 = 0.994$).

temperatures, the minimum value of $\chi_M T$ is 0.41 cm^3 K^{-1} mol^{-1}, suggesting an isotropic $S = {}^1/_2$ state. This conclusively illustrates that this nominally d^3 system does not possess a quartet ground state. This is further supported by electron paramagnetic resonance (EPR) spectroscopy data that are collected in section S.14. We are surprised to find that the $\chi_M T$ value increases linearly with temperature above 50 K, inconsistent with the curvature anticipated for (weaker) antiferromagnetic exchange coupling between metal and ligand spin centers. We attribute the linear response to temperature-independent magnetism (TIP) that results from second-order Zeeman coupling between the ground and excited states. The magnetic susceptibility of $[V(bpy)_3](ClO_4)_2$ has previously been reported, and its $\chi_M T$ is 1.79 cm^3 mol^{-1} K^{-1}, which is comparable with an $S = {}^3/_2$ spin-only value of 1.88 cm^3 mol^{-1} K^{-1}.[107] The temperature dependence of the magnetic susceptibility provided therein does not support the presence of TIP. Analogous magnetic properties of $[V(bpy)_3](ClO_4)_2$ are observed for Cr^{3+} and Mn^{4+} complexes, which suggests the electronic structure of $[\mathbf{1\text{-}CO_2Me}]^{2+}$ is unique with respect to other $3d^3$ transition metal complexes because of its $S = {}^1/_2$ ground state and large TIP.

While the TIP value is 15−20 times larger than is traditionally assigned to representative octahedral Co^{3+} complexes,[108] our assignment is consistent with previous reports of redox noninnocent octahedral Ti^{3+} and V^{4+} diimine systems whose anomalous magnetic properties were attributed to trigonal distortion.[109,110] The magnitude of TIP is inversely proportional to the excited state energies. Because of the redox-active transition metal center and ligand sets, $[\mathbf{1\text{-}CO_2Me}]^{2+}$ has a densely populated excited state manifold. This is detailed with respect to the NEVPT2(3,8) multireference calculations of $[\mathbf{1\text{-}CO_2Me}]^{2+}$ that are collected in Table S9 and Figure S17. Unless otherwise stated, the V−N_{bridge} bond length of the lowest-lying doublet state of the V^{2+} complexes was constrained during the DFT geometry optimization to the crystallographic distance of 2.25 Å.

The electronic absorption spectra of $[\mathbf{1\text{-}H}]^{2+}$, $[\mathbf{1\text{-}H}]^{3+}$, $[\mathbf{1\text{-}CO_2Me}]^{2+}$, and our previously detailed polypyridyl analogue, $[V(bpy)_3](OTf)_2$, are collected in Figure 3.[36,37] Along with the ligand field transitions detailed above, $[\mathbf{1\text{-}H}]^{3+}$ contains a high-energy MLCT at 378 nm, consistent with the large ionization energy of the V^{3+} ion. The broad peak observed in the near-IR region is indicative of a $\pi^* \leftarrow \pi^*$ transition of a ligand radical that is consistent with the crystallographic structure of $[\mathbf{1\text{-}CO_2Me}]^{2+}$. Similarly, we assign the absorbance with a λ_{max} at 397 nm to the V^{3+} MLCT that is red-shifted with respect to the unsubstituted complex, $[\mathbf{1\text{-}H}]^{3+}$. The TD-DFT results and NT$\rho^{\alpha,\beta}$ plots are provided in section S.7.2 and Figure S15.

Interestingly, we find that $[\mathbf{1\text{-}CO_2Me}]^{2+}$ displays spectroscopic signatures that are diagnostic of both V^{2+} and V^{3+} formal oxidation states. Along with the ligand field transitions detailed above, $[\mathbf{1\text{-}H}]^{3+}$ contains a high-energy MLCT at 378 nm, consistent with the large ionization energy of the V^{3+} ion. We assign the absorbance of $[\mathbf{1\text{-}CO_2Me}]^{2+}$ with a λ_{max} at 397 nm that we attribute to the V^{3+} MLCT. The broad peak observed in the near-IR region is indicative of a $\pi^* \leftarrow \pi^*$ transition of a ligand radical between the reduced and an unreduced iminopyridine group. Both spectroscopic features are consistent with the crystallographic structure of $[\mathbf{1\text{-}CO_2Me}]^{2+}$. The intense absorbance at 785 nm resembles the MLCT of $[\mathbf{1\text{-}H}]^{2+}$ whose energy is red-shifted by 0.12 eV. This suggests that both $^4A_2$ and the crystallographically and magnetically observed doublet state are present in solution. We corroborate this proposal with NEVPT2(3,8) calculations of $[\mathbf{1\text{-}CO_2Me}]^{2+}$ in its doublet and quartet optimized geometries that are collected in Figure S18. We do not observe a thermal dependence of the electronic absorbance in a 1:4 (v:v) methanol/ethanol mixture at 298 and 77 K that could be attributed to the solvatochromism that is detailed in sections S3.2 and S3.3. We calculate that the enthalpy of the unconstrained optimized geometry of the $[\mathbf{1\text{-}CO_2Me}]^{2+}$ doublet state of is 1.83 kcal mol^{-1} higher in energy than its quartet state. The unconstrained optimization lengthens the V−N_{bridge} bond from 2.21 to 2.42 Å and lowers the enthalpy of the doublet state by −2.85 kcal mol^{-1}. We note that hybrid DFT functionals routinely overstabilize spin states of greater multiplicity, which supports our proposal that the quartet and doublet states of $[\mathbf{1\text{-}CO_2Me}]^{2+}$ are nearly degenerate.[111,112]

The experimentally observed absorption at 467 nm is distinct to $[\mathbf{1\text{-}CO_2Me}]^{2+}$. The low energy of the transition suggests that the excitation is of triplet, rather than singlet, character that is magnetically coupled to the three-electron paramagnetic system. The absorbance values of nominally spin-forbidden transitions in aromatic systems have been previously reported in the presence of O_2 and attributed to their triplet ground states.[113] We follow up our TD-DFT study

https://doi.org/10.1021/acs.inorgchem.1c03418
Inorg. Chem. 2022, 61, 6376−6391

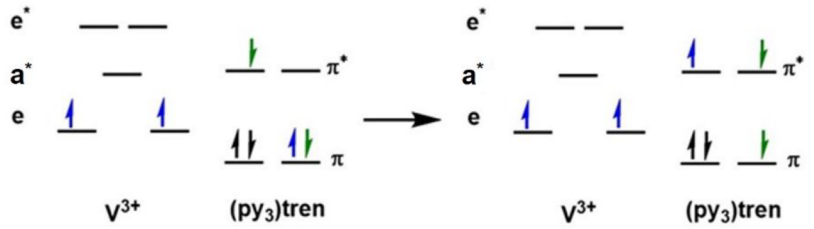

Figure 10. Orbital depiction of the ground and excited states of the intraligand $^2(^3\text{IL})$ transition of $[\mathbf{1\text{-}CO_2Me}]^{2+}$.

with an NEVPT2(5,5) study to address the multireference character of this transition. The resulting spin eigenfunctions for this excited state suggest that the reduced iminopyridine undergoes a spin flip during the transition that changes its magnetic coupling with the V^{3+} metal center from an antiferromagnetic (^{2}MLCT) to a ferromagnetic (^{4}MLCT) interaction that is detailed in Table S14. The ^{4}MLCT state antiferromagnetically couples with the triplet-intraligand transition (^{3}IL), resulting in an overall doublet state whose absorbance is spin allowed; we refer to it as $^2(^3\text{IL})$, and its orbital depiction is provided in Figure 10.

The cyclic voltammogram of $[\mathbf{1\text{-}CO_2Me}]^{2+}$, shown in Figure 9, resembles those of $[\mathbf{1\text{-}H}]^{2+}$ and $[\mathbf{1\text{-}H}]^{3+}$. $[\mathbf{1\text{-}CO_2Me}]^{2+}$ is oxidized at −0.39 V and reduced at −0.73 V versus Fc^+/Fc^0. The $E_{1/2}(3+/2+)$ and $E_{1/2}(2+/1+)$ redox events of compound $[\mathbf{1\text{-}CO_2Me}]^{2+}$ are 0.12 and 0.36 V anodic relative to the parent compounds, respectively, which we attribute to the electron-withdrawing properties of the ester substituents. Importantly, the open circuit potential does not sit at the $E_{1/2}$ value of the observed peaks, which suggests that there is one dominant species in solution and no impurity, such as a di- and tricationic reduced−oxidized pair. The $E_{1/2}(3+/2+)$ redox event displays quasi-reversibility, consistent with the electrochemical behavior of $[\mathbf{1\text{-}H}]^{3+}$. This suggests that $[\mathbf{1\text{-}CO_2Me}]^{2+}$ maintains the crystallographically observed capped octahedral geometry in solution. The similar electrochemical properties suggest that the products of both reduction and oxidation of $[\mathbf{1\text{-}H}]^{2+}$ and $[\mathbf{1\text{-}CO_2Me}]^{2+}$ are analogous, which is supported by spectroelectrochemistry data that are provided in section S2.2. The data suggest that the structural features of $[\mathbf{1\text{-}H}]^{2+}$ and $[\mathbf{1\text{-}CO_2Me}]^{2+}$ are attributable to different electronic states of the +2 system, which correspond to the lowest-lying quartet and doublet states of a $3d^3$ system, respectively.

Treatment of Multielectron Antiferromagnetism with the SOAP Method. To elucidate this complex spin system, we expand upon Hund's first rule and consider the electronic structure of the doublet ground state of $[\mathbf{1\text{-}CO_2Me}]^{2+}$ that can be described in local terms as a V^{3+} (d^2) metal center and anionic ligand radical (π^{*-}).

The metal center's two unpaired electrons and anionic ligand radical occupy nondegenerate orbitals that can be antiferromagnetically coupled, the doublet being lower in energy than the quartet state. Both solid state and molecular models of antiferromagnetic coupling require overlap between magnetic orbitals.[114−117] Orbital orthogonality is a requirement of most electronic structure methods, spin unrestricted broken symmetry models being the exception.[118−120] The overlap between unpaired electrons that engender antiferromagnetic coupling can be found by using multideterminant methods. Multireference NEVPT2(3,8) calculations suggest that the doublet ground state is stabilized by 0.55 eV with respect to the ^{4}MLCT state, that is equal to a magnetic coupling of $J = -1480\ \text{cm}^{-1}$ with respect to a $-2J$ formalism for the Heisenberg−Dirac−van Vleck Hamiltonian.[84,85]

We describe an antiferromagnetic interaction as a configuration interaction involving metal-centered (φ_a) and an anionic ligand radical (φ_b) orbital that are partially occupied. φ_a and φ_b are orthogonal one-electron wave functions.[48,49,51,121] This is detailed in eq 6, where the pair coefficients (c_1 and c_2) are solved variationally with respect to the lowest-energy doublet state. The first configuration by itself is termed a perfect pairing model in which electrons that are singlet-coupled are orthogonal to the spatial and spin wave functions of the system's remaining electrons.[50] Our SOAP method expands on this conventional description of two electrons[117] by addressing the spin recoupling involving the remaining metal-centered unpaired electron (φ_c).[122] This recoupling is accomplished with inclusion of a third configuration in eq 6, where φ_a and φ_b are triplet coupled via their magnetic interaction with φ_c. The spin coefficients (ε_1 and ε_2) are normalized with respect to the two spin eigenfunctions that are shown in eq 6, where α and β are electron spins.

$$\psi(\text{SOAP}) = \varepsilon_1[(c_1\phi_a\phi_a - c_2\phi_b\phi_b)\phi_c](\alpha\beta - \beta\alpha)\alpha + \varepsilon_2[(\phi_a\phi_b - \phi_b\phi_a)\phi_c](2\alpha\alpha\beta - \alpha\beta\alpha - \beta\alpha\alpha) \quad (6)$$

The coupling between this new configuration and a perfect pairing model is provided by the meta-exchange interaction (M_c) in eqs 7 and 8. This electron−electron interaction reflects the overlap between the overlap functionals that involve the third unpaired electron (f_{ac} and f_{bc}). If the three orbitals are mutually orthogonal, then the energy expression of eq 6 simplifies to the ^{2}E excited state energy detailed with respect to $[\mathbf{1\text{-}H}]^{2+}$.

$$M_c = \int\int \frac{\phi_a(1)\phi_c(1)\phi_b(2)\phi_c(2)}{r_{12}}\,dr_1\,dr_2 \quad (7)$$

$$M_c = \int\int \frac{f_{ac}f_{bc}}{r_{12}}\,dr_1\,dr_2 \quad (8)$$

For visualization and insight, the two paired orthogonal orbitals φ_a and φ_b can be transformed into equivalent nonorthogonal one-electron wave functions, φ_x and φ_y, respectively, as detailed in eqs 9−11 with respect to the pair coefficients c_1 and c_2. The resulting overlap of φ_x and φ_y in the SOAP wave function is 0.23, which classifies $[\mathbf{1\text{-}CO_2Me}]^{2+}$ as showing an antiferromagnetic coupling, rather than a covalent bond, between its V^{3+} metal center and anionic ligand radical. Our calculated nonorthogonal orbitals of $[\mathbf{1\text{-}CO_2Me}]^{2+}$ are presented in Figure 11, along with their originating orthogonal orbitals from the SCF framework. Our SOAP method assigns

https://doi.org/10.1021/acs.inorgchem.1c03418
Inorg. Chem. 2022, 61, 6376−6391

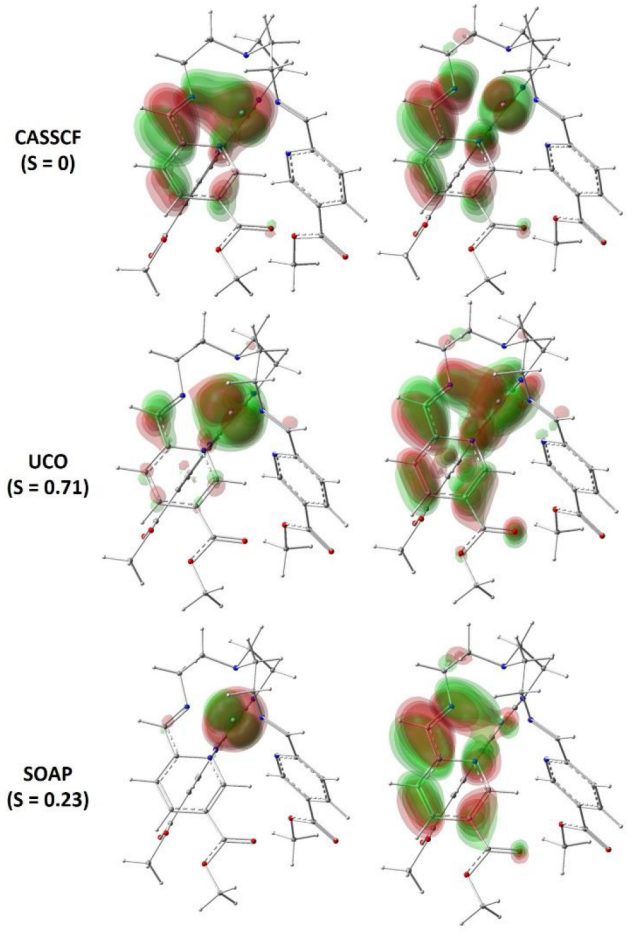

Figure 11. Singly occupied orbitals that describe the antiferromagnetic coupling of the vanadium complex in $[\mathbf{1\text{-}CO_2Me}]^{2+}$. This is presented as orthogonal bonding (φ_a) and antibonding (φ_b) orbitals (top) with respect to the state specific CASSCF(3,3) wave function of the lowest-lying doublet. Unrestricted corresponding orbitals (UCO's) of the TPSSh BS-DFT wave function (middle). Equations 9 and 10 transform those orbitals into nonorthogonal and localized metal-centered (φ_x) and anionic ligand radical (φ_y) orbitals (bottom) with respect to their calculated pair coefficients, c_1 and c_2. The overlap between the two orbitals (S) is provided in parentheses with respect to their pair coefficients illustrated in eq 11. The contours are shown from 0.025 to 0.045 in increments of 0.01 electron bohr^{-2}.

an antiferromagnetic coupling of $J = -1490$ cm^{-1} that accurately reproduces the sign and magnitude of the magnetic coupling of $[\mathbf{1\text{-}CO_2Me}]^{2+}$ (the energy expressions are further detailed in section S7.2). We also use the broken symmetry method (BS-DFT) with the TPSSh hybrid-DFT functional to calculate the magnetic coupling of $[\mathbf{1\text{-}CO_2Me}]^{2+}$. The TPSSh functional has been shown to accurately treat the spin state energetic of diverse multielectron systems.[123,124] The DFT-BS procedure calculates a J of -1600 cm^{-1} that is consistent with the methods detailed above. The unrestricted corresponding orbital (UCO) transformation of the DFT-BS wave function assigns an overlap of 0.70 for the nonorthogonal electron pair that is shown in Figure 11. We attribute the larger calculated overlap for the UCO transformation (with respect to our SOAP method) to its lack of accounting for the third spin coupling configuration detailed in eq 6.

$$\phi_x = \frac{\sqrt{c_1}\phi_a + \sqrt{c_2}\phi_b}{\sqrt{c_1 + c_2}} \tag{9}$$

$$\phi_y = \frac{\sqrt{c_1}\phi_a - \sqrt{c_2}\phi_b}{\sqrt{c_1 + c_2}} \tag{10}$$

$$S = \frac{c_1 - c_2}{c_1 + c_2} \tag{11}$$

The observation of a doublet electronic configuration as the ground state is unique to $[\mathbf{1\text{-}CO_2Me}]^{2+}$ with respect to $[\mathbf{1\text{-}H}]^{2+}$. To improve our understanding of this, we consider the NEVPT2(3,8) transitions of the quartet-optimized geometry of $[\mathbf{1\text{-}CO_2Me}]^{2+}$, which is consistent with a local V^{2+} metal center, analogous to the crystallographic structure of $[\mathbf{1\text{-}H}]^{2+}$. On the basis of analogous Cr^{3+} complexes, we would expect to observe five near-degenerate low-lying doublets that are attributed to the metal-centered ^{2}E and (^{2}E + ^{2}A$_2$) states of a C_3-symmetric d^3 system. However, as previously reported for $[V^{2+}(bpy)_3]$,[36] we calculate six doublet states that are below approximately 1.5 eV for both $[\mathbf{1\text{-}H}]^{2+}$ and $[\mathbf{1\text{-}CO_2Me}]^{2+}$. The states exhibit significant multireference mixing between the metal-centered and π^* orbitals, which describe resonance stabilization and static correlation. Rather than dominantly metal-based states, the doublet excited states exhibit coupling between their metal-centered and charge transfer states that we term ^{2}MC/^{2}MLCT.[36] The CASSCF(3,8) wave function determines that the ^{2}MC and ^{2}MLCT state functions contribute approximately equally to the lowest-lying doublet excited state for both $[\mathbf{1\text{-}H}]^{2+}$ and $[\mathbf{1\text{-}CO_2Me}]^{2+}$, whose excited state energies are 1.05 and 0.88 eV, respectively.

We also observe a low-lying ^{4}MLCT state, strongly stabilized by dynamic correlation, that is 1.75 and 0.74 eV above the ground states for $[\mathbf{1\text{-}H}]^{2+}$ and $[\mathbf{1\text{-}CO_2Me}]^{2+}$, respectively. Heptacoordination with the tren scaffold and antiferromagnetic coupling with the iminopyridine anionic ligand radical in the doublet ground state geometry should collectively stabilize the doublet configuration by approximately 1.2 eV. These features place the energy of the ^{2}MLCT excited state below that of the ^{4}A$_2$ ground state for $[\mathbf{1\text{-}CO_2Me}]^{2+}$, which would not be observed in the case of $[\mathbf{1\text{-}H}]^{2+}$. Relative to the parent ligand set, we calculate that the 5-CO_2Me substituent stabilizes the electron affinity of the uncoordinated ligand by 0.58 eV. Rotating the ester substituent so that its π-system is orthogonal to the iminopyridine ligand set diminishes the electron affinity stabilization to -0.18 eV. This suggests that the ester substituent serves as a π-acid that stabilizes the charge transfer state of $[\mathbf{1\text{-}CO_2Me}]^{2+}$, resulting in the relative energies of the lowest-lying quartet and doublet states.

CONCLUSIONS AND OUTLOOK

We have established that the doublet ground state of $[\mathbf{1\text{-}CO_2Me}]^{2+}$ is stabilized by a large electron affinity for the *m*-methyl ester-substituted iminopyridine, strong antiferromagnetic coupling with the anionic ligand radical, and heptacoordination with the tren scaffold. Concurrently, the stability of the ferromagnetic quartet state is decreased due to the delocalization of its metal-centered orbitals, which weakenes exchange interactions. Stabilization of the doublet ground state is further attributed to the electronic coupling, resonance stabilization, between the doublet metal-centered (^{2}MC) and metal-to-ligand charge transfer (^{2}MLCT), which

https://doi.org/10.1021/acs.inorgchem.1c03418
Inorg. Chem. 2022, 61, 6376−6391

we term ^{2}MC/^{2}MLCT. Collectively, these features combine to invert the ground and excited states for [**1-CO$_2$Me**]$^{2+}$, as observed crystallographically, spectroscopically, and magnetically.

States of distinct multiplicities are differentially impacted by resonance. This is foundational to chemistry, the Heitler–London treatment of H_2 assigning resonance and configuration interactions as the basis of the attractive and dominantly repulsive character of its singlet ($\alpha\beta$) and triplet ($\alpha\alpha$) states, respectively.[125] While intuitive for a covalent bond, resonance in the ground states of paramagnetic coordination complexes is relatively obscured. The stability of the high-spin state for [**1-CO$_2$Me**]$^{2+}$ predicted from Hund's first rule is complicated by nondegenerate and nonorthogonal orbitals that possess competing magnetic interactions.[126] Herein, we uncover a unique phenomenon in which resonance stabilization causes an unexpected ground ($S = {}^1/_2$) state of a nominally V^{2+} ($3d^3$) transition metal complex.

The conditions for this doublet ground state to manifest are perfectly satisfied with the ligand environment of [**1-CO$_2$Me**]$^{2+}$. Alvarez has previously performed an extensive characterization of the crystallographic structures of heptacoordinate transition metal complexes.[62] Heptacoordinate structures are largely observed in group 3–6 elements with a d^0–d^4 electronic population whose conditions are met for $V^{2+/3+}$. While the geometry of heptacoordinate structures is traditionally dynamic, possessing low barriers of conversion, the C_3 symmetry and multidentate chelation of the tren scaffold enables achievement of a capped octahedral coordination environment.[127] Coordination between the V^{3+} metal center and bridgehead nitrogen stabilizes the doublet state by approximately 15 kcal mol^{-1}.

Lastly, the redox noninnocence of the iminopyridine groups provides [**1-CO$_2$Me**]$^{2+}$ a mechanism for accessing its doublet ground state. The strong electronic coupling between the metal-centered orbitals and anionic ligand radical results in resonance stabilization that assigns the ^{2}MC/^{2}MLCT as the electronic ground state. The ester substituent magnifies this effect, consistent with our previous studies of the emission properties of analogous Cr^{3+} complexes, which suggest greater metal–ligand covalency.[63,128]

We briefly summarize the advancements that our SOAP method affords for the theoretical treatment of open-shell systems. We note that, with select exceptions,[129−132] models for antiferromagnetism have focused on two-electron systems.[117] Because our method decomposes the magnetism of a system into its pairwise components, it can be employed to assign competing magnetic interactions in a multielectron system.[133,134] We establish that metal–ligand covalency affects the magnitude of electron–electron exchange interactions, thus modulating the strength of the high-spin (ferromagnetic) state. Greater metal–ligand covalency concurrently stabilizes charge transfer states in the molecule. The observation of the $^4A_2$ and ^{2}MC/^{2}MLCT ground states for [**1-H**]$^{2+}$ and [**1-CO$_2$Me**]$^{2+}$, respectively, alludes to a promising design principle for stabilizing the doublet ground state based on established synthetic principles of ligand substituent electronics. An analogous proposal for stabilizing the quartet state has recently been made by Wenger.[9]

The variational approach of our SOAP method can address the avenues for resonance stabilization and magnetic coupling that are accessible to open-shell systems. This feature also provides the opportunity to transform computationally convenient orthogonal orbitals to nonorthogonal orbitals, orbital overlap being the requirement for antiferromagnetic coupling. From a practical standpoint, the calculation time of the interelectronic terms scales with the volume of an orbital's grid rather than the total number of electrons. Because the only required input is the Gaussian cube of a system's singly occupied orbitals, the procedure is agnostic to the originating electronic structure software.

EXPERIMENTAL SECTION

Physical Methods. Absorption spectra were recorded with a Hewlett-Packard 8453 spectrometer in quartz cuvettes with a 1 cm path length. Infrared spectra were recorded with either a Nicolet 380 FT-IR or a Bruker TENSOR II spectrometer. Mass spectrometry measurements were performed in positive ion or negative ion mode on a Thermo-Finnigan LTQ mass spectrometer equipped with an analytical electrospray ion source using a spray voltage of 2.5 V and a capillary temperature of 175 °C.

Preparation of Compounds. Manipulations and syntheses of all metal complexes were performed inside a dinitrogen-filled glovebox (MBRAUN Labmaster 130). All solvents were sparged with dinitrogen, passed over molecular sieves, and degassed prior to use. The compounds [V(CH$_3$CN)$_6$](OTf)$_2$,[135] (py$_3$)tren,[136] and (5-CO$_2$Mepy)$_3$tren[87] were all prepared according to literature procedures.

Compound [**1-H**](**OTf**)$_2$ can be generated under multiple conditions, although we have found that the choice of starting material influences the purity of the products. Use of the V^{3+} starting material [V(CH$_3$CN)$_6$Cl$_3$] affords a green solution with electronic absorption properties similar to those of compound [**1-H**](**OTf**)$_2$ as measured in CH$_3$CN. When the reaction solution is changed from acetonitrile to tetrahydrofuran, a brown product resembling compound [**1-H**](**OTf**)$_3$ is produced. The yield of [**1-H**](**OTf**)$_3$ increases with a decrease in temperature as reactions carried out at −77 °C afford ∼88% of the crude brown precipitate. Due to these complications, we investigated [V(CH$_3$CN)$_6$](BPh$_4$)$_2$ as a V^{2+} starting material. We found [V(py)$_3$tren]$^{2+}$ is present on the basis of the electronic absorption spectrum, but the molar absorptivity is much lower than that of compound [**1-H**](**OTf**)$_2$ in the same solvent, indicating a mixture of products. Eventually, we found compound [**1-H**](**OTf**)$_2$ to be readily prepared as a pure compound by using the starting material [V(CH$_3$CN)$_6$](OTf)$_2$, according to the procedure described below (Scheme 1).

*[V(py$_3$)tren](OTf)$_2$ [[**1-H**](**OTf**)$_2$].* A green solution of [V(CH$_3$CN)$_6$](OTf)$_2$ (629 mg, 1.06 mmol) and (py$_3$)tren (444 mg, 1.08 mmol) in 8 mL of CH$_3$CN was stirred for 4 h. The solvent was removed under reduced pressure and washed with diethyl ether (3 × 3 mL) to afford a green powder. Dark green plate crystals were grown via diffusion of a diethyl ether into a concentrated solution of CH$_3$CN to yield 665 mg (0.872 mmol, 83% yield) of dark green plate crystals: UV–vis (CH$_3$CN) λ_{max} (nm) [ε_M (M^{-1} cm^{-1})] 213 (19967), 276 (17362), 402 (1978), 655 (3836), 729 (5219); IR (KBr pellet) $\nu_{C=N}$ 1599 cm^{-1}; ESI-MS(+) (CH$_3$CN) m/z 232.09 ([**1-H**](**OTf**)$_2$ − 2OTf$^-$)$^{2+}$. Anal. Calcd for $C_{26}H_{27}F_6N_7O_6S_2V$ [[**1-H**](**OTf**)$_2$]: C, 40.95; H, 3.57; N, 12.86. Found: C, 40.87; H, 3.56; N, 12.84.

*[V(py$_3$)tren](OTf)$_3$ [[**1-H**](**OTf**)$_3$].* A clear solution of AgOTf (129 mg, 0.503 mmol) in 3 mL of CH$_3$CN was added to a solution of [V(py$_3$)tren](OTf)$_2$ (383 mg, 0.502 mmol) in 8 mL of CH$_3$CN. Immediately, a Ag precipitate was observed as the color of the solution changed from green to brown. The mixture was stirred for 1 h. The reaction mixture was filtered through Celite to remove Ag metal, and the filtrate was concentrated under reduced pressure. Crystals were grown from diffusion of diisopropyl ether into a concentrated CH$_3$CN solution to yield 303 mg (0.332 mmol, 66% yield) of brown needle crystals: UV–vis (CH$_3$CN) λ_{max} (nm) [ε_M (M^{-1} cm^{-1})] 288 (15200), 369 (3760), 449 (788), 506 (351), 774 (26); IR (KBr pellet) $\nu_{C=N}$ 1605 cm^{-1}; ESI-MS(+) (CH$_3$CN) m/z 154.75 ([**1-H**] − 3OTf$^-$)$^{3+}$, 762.09 ([**1-H**](**OTf**)$_3$ − 2OTf$^-$)$^{2+}$. Anal.

https://doi.org/10.1021/acs.inorgchem.1c03418
Inorg. Chem. 2022, 61, 6376−6391

Scheme 1. Preparation of [1-H](OTf)$_2$, [1-H](OTf)$_3$, and [1-CO$_2$Me](OTf)$_2$

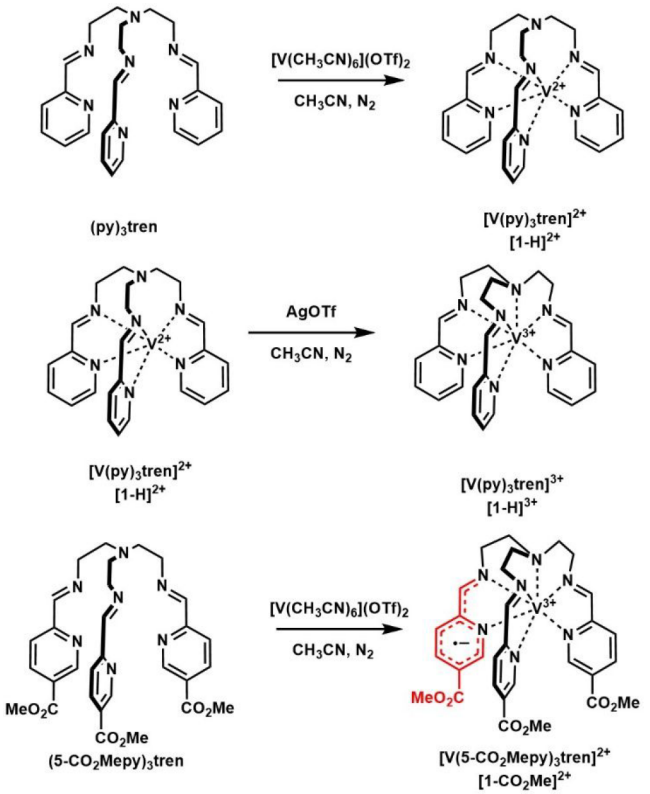

Calcd for $C_{27}H_{27}F_9N_7O_9S_3V$ [[**1-H**](**OTf**)$_3$]: C, 35.57; H, 2.99; N, 10.75. Found: C, 35.44; H, 3.01; N, 10.78.

[V(5-CO$_2$Mepy$_3$)tren](OTf)$_2$ [[1-CO$_2$Me](OTf)$_2$]. A solution of [V(CH$_3$CN)$_6$](OTf)$_2$ (242 mg, 0.406 mmol) and the ligand (5-CO$_2$Mepy$_3$)tren (240 mg, 0.408 mmol) in 8 mL of CH$_3$CN was stirred for 4 h. The solvent was removed under reduced pressure and washed with diethyl ether (3 × 3 mL). Crystals were grown from diffusion of diethyl ether into a concentrated solution of methanol to yield 195 mg (0.208 mmol, 51% yield) of black plate crystals: UV−vis (CH$_3$CN) λ_{max} (nm) [ε_M (M^{-1} cm^{-1})] 205 (55300), 236 (37500), 287 (29900), 396 (4620), 667 (3900), 785 (5440), 1024 (1210); IR (KBr pellet) $\nu_{C=O}$ 1725 cm^{-1}, $\nu_{C=N}$ 1600 cm^{-1}; ESI-MS(+) (CH$_3$CN) *m/z* 319.25 ([**1-CO$_2$Me**](**OTf**)$_2$ − 2OTf$^-$)$^{2+}$. Anal. Calcd for $C_{32}H_{33}F_6N_7O_{12}S_2V$ [[**1-CO$_2$Me**](**OTf**)$_2$]: C, 41.03; H, 3.55; N, 10.47. Found: C, 40.68; H, 2.72; N, 10.42.

Crystallography. Key structural data for compounds [**1-H**](**OTf**)$_2$, [**1-H**](**OTf**)$_3$, and [**1-CO$_2$Me**](**OTf**)$_2$ are listed in Table S1. Crystals were coated in Paratone oil, supported on Cryoloops, and mounted on either a Bruker Kppa Apex 2 instrument with a CCD diffractometer [[**1-H**](**OTf**)$_2$] or a Bruker D8 Quest ECO instrument with a Photon 50 CMOS diffractometer [[**1-H**](**OTf**)$_3$ and [**1-CO$_2$Me**](**OTf**)$_2$] under a stream of cold nitrogen. All data collections were performed with Mo Kα radiation and a graphite monochromator. Initial lattice parameters were determined from a minimum of 310 reflections harvested from 24 frames; these parameters were later refined against all data. Data sets were collected targeting full coverage and 4-fold redundancy. Data were integrated and corrected for absorption effects with the APEX 3 software packages. Structures were determined by direct methods and refined with the SHELXTL software package. Displacement parameters for all non-hydrogen atoms were refined anisotropically. All hydrogens were assigned to ideal positions and refined using a riding model with an isotropic thermal parameter 1.2 times greater than that of the attached carbon atom.

Electrochemistry. Voltammograms (Figure 8) were recorded with either a CH Instruments 1230A or a Gamry Reference 600 potentiostat under a dinitrogen/argon atmosphere. All experiments used a 0.1 M tetrabutylammonium hexafluorophosphate (Bu_4NPF_6) solution in an acetonitrile with a 0.25 mm Pt disk working electrode, a Ag wire quasi-reference electrode, and a Pt wire auxiliary electrode. Reported potentials (Table S2) are referenced to the ferrocenium/ferrocene {[(C$_5$H$_5$)$_2$Fe]$^+$/[(C$_5$H$_5$)$_2$Fe], $Fc^{+/0}$} redox couple and were determined by adding ferrocene as an internal standard at the conclusion of each electrochemical experiment.

Magnetic Measurements. Solid state magnetic property data for compound [**1-CO$_2$Me**](**OTf**)$_2$ were collected using a Quantum Design MPMS XL SQUID magnetometer. Powdered microcrystalline samples were loaded into polyethylene bags and inserted into a straw before being transported to the magnetometer. The presence of ferromagnetic impurities was probed by a variable field analysis (0 to 10 kOe) of the magnetization at 100 K (Figure S10). The lack of curvature in the plots of *M* versus *H* for [**1-CO$_2$Me**](**OTf**)$_2$ indicate the absence of significant ferromagnetic impurities. Magnetic susceptibility data were collected at temperatures ranging from 2 to 300 K. Data were corrected for the diamagnetic contributions of the sample holder and bag by subtracting empty containers. Corrections for the sample were calculated from Pascal's constants.[137]

Computational Procedure. The following calculations were performed with the Gaussian16 electronic structure software package.[138] We employed the APFD hybrid DFT functional[139] and a 6-311+g(d) basis set[140] with its parametrized empirical dispersion correction in a PCM acetonitrile continuum solvent.[141] The quartet and doublet states of [**1-H**](**OTf**)$_2$ and [**1-CO$_2$Me**](**OTf**)$_2$ were optimized where the V−N$_{bridge}$ separation was constrained to their crystallographic values of 3.15 and 2.21 Å, respectively. The structure of [**1-H**](**OTf**)$_3$ was optimized as a triplet with no geometric constraints.[66] The uncoordinated iminopyridine ligand sets were optimized where the torsion of the bidentate binding group was constrained at 0° for the neutral and singly reduced (monoanionic) states.

A frequency analysis was performed on the quartet and doublet states of [**1-CO$_2$Me**]$^{2+}$. We report a single imaginary frequency along the constrained V−N$_{bridge}$ bond of the doublet state. The unconstrained optimization of the [**1-CO$_2$Me**]$^{2+}$ state removes the imaginary frequency and decreases the system's enthalpy by −2.9 kcal mol^{-1}. This suggests that the vibrational mode has a soft potential energy. We also report that the bond length increases from the crystallographic value of 2.21 to 2.42 Å. Our calculations refer to the [**1-CO$_2$Me**]$^{2+}$ crystallographic V−N$_{bridge}$ bond length unless otherwise stated.

The energy of the ^{2}E excited state with respect to the quartet geometry of [**1-H**](**OTf**)$_2$ and [**1-CO$_2$Me**](**OTf**)$_2$ was multiplied by a factor of $^3/_2$ to account for the single-determinant character of the DFT-based wave function. The foundation of our multideterminant DFT correction has been detailed elsewhere.[37] The doublet wave function was verified as the ground state through the use of a wave function stability check: single excitations with respect to the trial wave function were included to test for a lower-energy solution, the 'stable=opt' command in g16.

The following calculations were performed with the ORCA 4.1 electronic structure software program.[86] We used multireference techniques with a CASSCF(3,8) model in which the active space was selected to be the five 3d orbitals and the three lowest-lying π^* orbitals. The def2-TZVP and def2-TZVPP basis sets[142] were used for the non-metal and metal atoms, respectively, with a CPCM acetonitrile continuum solvent. The final energies for the excited states were obtained with the NEVPT2 technique with the same active space and conditions.[83−85]

The electron−electron integrals detailed for our SOAP method were calculated, and their cubes generated from their CASSCF(3,8) orbitals that were state specific with respect to their electronic ground state. We selected a grid size of 90 × 90 × 90 for fine resolution. The orbital energies of the magnetic orbitals were approximated from the converged Restricted Open Hartree−Fock (ROHF) wave function of the quartet state. The coefficients used for the SO method (A_1−A_3)

https://doi.org/10.1021/acs.inorgchem.1c03418
Inorg. Chem. 2022, 61, 6376−6391

were obtained from the lowest-lying doublet of the corresponding CASSCF(3,3) wave function.

The continuous shape measures (CShM) of the experimental crystallographic coordinates and DFT-optimized geometries were evaluated with SHAPE version 2.2.[56]

■ ASSOCIATED CONTENT

Supporting Information

The Supporting Information is available free of charge at https://pubs.acs.org/doi/10.1021/acs.inorgchem.1c03418.

Crystal structure details, Randles−Sevcik analysis, spectroelectrochemistry, temperature-dependent UV−vis, electronic absorbance solvatochromism, magnetic measurements, geometry-optimized total energies, TD-DFT, NT$\rho^{\alpha,\beta}$ plots, NEVPT2(3,8) transition energies, CASSCF(3,8) active space orbitals, procedure for the SOAP method and calculating doublet energies of three-electron systems (PDF)

Cartesian coordinates of the DFT geometry-optimized complexes (ZIP)

Accession Codes

CCDC 2114725−2114727 contain the supplementary crystallographic data for this paper. These data can be obtained free of charge via www.ccdc.cam.ac.uk/data_request/cif, or by emailing data_request@ccdc.cam.ac.uk, or by contacting The Cambridge Crystallographic Data Centre, 12 Union Road, Cambridge CB2 1EZ, UK; fax: +44 1223 336033.

■ AUTHOR INFORMATION

Corresponding Authors

Anthony K. Rappé − *Department of Chemistry, Colorado State University, Fort Collins, Colorado 80523, United States;* orcid.org/0000-0002-5259-1186; Email: anthony.rappe@colostate.edu

Matthew P. Shores − *Department of Chemistry, Colorado State University, Fort Collins, Colorado 80523, United States;* orcid.org/0000-0002-9751-0490; Email: matthew.shores@colostate.edu

Authors

Justin P. Joyce − *Department of Chemistry, Colorado State University, Fort Collins, Colorado 80523, United States;* orcid.org/0000-0002-8287-622X

Romeo I. Portillo − *Department of Chemistry, Colorado State University, Fort Collins, Colorado 80523, United States*

Complete contact information is available at: https://pubs.acs.org/10.1021/acs.inorgchem.1c03418

Author Contributions

[||]J.P.J. and R.I.P. are co-first authors and contributed equally to this work. J.P.J. and A.K.R. provided theoretical methods. R.I.P. and M.P.S. performed and/or interpreted the experimental results unless stated otherwise in the Acknowledgments. All of the authors contributed to the writing of the manuscript and have given approval to the final version of the manuscript.

Funding

This work was carried out by the Catalysis Collaboratory for Light-activated Earth Abundant Reagents (C-CLEAR), which was supported by the National Science Foundation (NSF) and the Environmental Protection Agency through the Networks for Sustainable Molecular Design and Synthesis (NSF-CHE-1339674). Support from NSF-CHE-1956399 is also acknowledged.

Notes

The authors declare no competing financial interest.

■ ACKNOWLEDGMENTS

The authors thank Dr. Brooke N. Livesay for refining the structures of the three detailed compounds. The authors also thank Anthony Campanella for assistance in interpreting the EPR spectrum of $[\mathbf{1\text{-}CO_2Me}](\mathbf{OTf})_2$.

■ REFERENCES

(1) Bullock, R. M.; Chen, J. G.; Gagliardi, L.; Chiri, P. J.; Farh, O. K.; Hendo, C. H.; Jone, C. W.; Keit, J. A.; Klosin, J.; Mintee, S. D.; Morri, R. H.; Radosevic, A. T.; Rauchfus, T. B.; Strotma, N. A.; Vojvodic, A.; War, T. R.; Yan, J. Y.; Surendranath, Y. Using Nature's Blueprint to Expand Catalysis with Earth-Abundant Metals. *Science* **2020**, *369* (6505), 3183 DOI: 10.1126/science.abc3183.

(2) McCusker, J. K. Electronic Structure in the Transition Metal Block and Its Implications for Light Harvesting. *Science* **2019**, *363* (6426), 484−488.

(3) Wenger, O. S. Photoactive Complexes with Earth-Abundant Metals. *J. Am. Chem. Soc.* **2018**, *140* (42), 13522−13533.

(4) Förster, C.; Heinze, K. Photophysics and Photochemistry with Earth-Abundant Metals-Fundamentals and Concepts. *Chem. Soc. Rev.* **2020**, *49* (4), 1057−1070.

(5) Herr, P.; Kerzig, C.; Larsen, C. B.; Häussinger, D.; Wenger, O. S. Manganese(I) Complexes with Metal-to-Ligand Charge Transfer Luminescence and Photoreactivity. *Nat. Chem.* **2021**, *13*, 956−962, DOI: 10.1038/s41557-021-00744-9.

(6) Reichenauer, F.; Wang, C.; Förster, C.; Boden, P.; Ugur, N.; Báez-Cruz, R.; Kalmbach, J.; Carrella, L. M.; Rentschler, E.; Ramanan, C.; Niedner-Schatteburg, G.; Gerhards, M.; Seitz, M.; Resch-Genger, U.; Heinze, K. Strongly Red-Emissive Molecular Ruby $[Cr(Bpmp)_2]^{3+}$ Surpasses $[Ru(Bpy)_3]^{2+}$. *J. Am. Chem. Soc.* **2021**, *143* (30), 11843−11855.

(7) McKone, J. R.; Marinescu, S. C.; Brunschwig, B. S.; Winkler, J. R.; Gray, H. B. Earth-Abundant Hydrogen Evolution Electrocatalysts. *Chem. Sci.* **2014**, *5* (3), 865−878.

(8) Yang, M.; Sheykhi, S.; Zhang, Y.; Milsmann, C.; Castellano, F. N. Low Power Threshold Photochemical Upconversion Using a Zirconium(IV) LMCT Photosensitizer. *Chem. Sci.* **2021**, *12* (26), 9069−9077.

(9) Wegeberg, C.; Wenger, O. S. Luminescent First-Row Transition Metal Complexes. *JACS Au* **2021**, *1* (11), 1860−1876.

(10) Hockin, B. M.; Li, C.; Robertson, N.; Zysman-Colman, E. Photoredox Catalysts Based on Earth-Abundant Metal Complexes. *Catal. Sci. Technol.* **2019**, *9* (4), 889−915.

(11) Frost, J. M.; Harriman, K. L. M.; Murugesu, M. The Rise of 3d Single-Ion Magnets in Molecular Magnetism: Towards Materials from Molecules? *Chem. Sci.* **2016**, *7* (4), 2470−2491.

(12) Gomez-Coca, S.; Cremades, E.; Aliaga-Alcalde, N.; Ruiz, E. Mononuclear Single-Molecule Magnets: Tailoring the Magnetic Anisotropy of First-Row Transition-Metal Complexes. *J. Am. Chem. Soc.* **2013**, *135* (18), 7010−7018.

(13) Craig, G. A.; Murrie, M. 3d Single-Ion Magnets. *Chem. Soc. Rev.* **2015**, *44* (8), 2135−2147.

(14) Atanasov, M.; Aravena, D.; Suturina, E.; Bill, E.; Maganas, D.; Neese, F. First Principles Approach to the Electronic Structure, Magnetic Anisotropy and Spin Relaxation in Mononuclear 3d-Transition Metal Single Molecule Magnets. *Coord. Chem. Rev.* **2015**, *289−290* (1), 177−214.

(15) Woodhouse, M. D.; McCusker, J. K. Mechanistic Origin of Photoredox Catalysis Involving Iron(II) Polypyridyl Chromophores. *J. Am. Chem. Soc.* **2020**, *142* (38), 16229−16233.

(16) Higgins, R. F.; Fatur, S. M.; Shepard, S. G.; Stevenson, S. M.; Boston, D. J.; Ferreira, E. M.; Damrauer, N. H.; Rappé, A. K.; Shores,

M. P. Uncovering the Roles of Oxygen in Cr(III) Photoredox Catalysis. *J. Am. Chem. Soc.* **2016**, *138* (16), 5451−5464.
(17) Bagal, D. B.; Kachkovskyi, G.; Knorn, M.; Rawner, T.; Bhanage, B. M.; Reiser, O. Trifluoromethylchlorosulfonylation of Alkenes: Evidence for an Inner-Sphere Mechanism by a Copper Phenanthroline Photoredox Catalyst. *Angew. Chem., Int. Ed.* **2015**, *54* (24), 6999−7002.
(18) Strieth-Kalthoff, F.; James, M. J.; Teders, M.; Pitzer, L.; Glorius, F. Energy Transfer Catalysis Mediated by Visible Light: Principles, Applications, Directions. *Chem. Soc. Rev.* **2018**, *47* (19), 7190−7202.
(19) Arias-Rotondo, D. M.; McCusker, J. K. The Photophysics of Photoredox Catalysis: A Roadmap for Catalyst Design. *Chem. Soc. Rev.* **2016**, *45* (21), 5803−5820.
(20) Twilton, J.; Le, C.; Zhang, P.; Shaw, M. H.; Evans, R. W.; MacMillan, D. W. C. The Merger of Transition Metal and Photocatalysis. *Nat. Rev. Chem.* **2017**, *1* (7), 52 DOI: 10.1038/s41570-017-0052.
(21) Gaffney, K. J. Capturing Photochemical and Photophysical Transformations in Iron Complexes with Ultrafast X-Ray Spectroscopy and Scattering. *Chem. Sci.* **2021**, *12* (23), 8010−8025, DOI: 10.1039/D1SC01864G.
(22) Sánchez-Murcia, P. A.; Nogueira, J. J.; Plasser, F.; González, L. Orbital-Free Photophysical Descriptors to Predict Directional Excitations in Metal-Based Photosensitizers. *Chem. Sci.* **2020**, *11* (29), 7685−7693.
(23) Crandell, D. W.; Muñoz, S. B.; Smith, J. M.; Baik, M.-H. Mechanistic Study of Styrene Aziridination by Iron(IV) Nitrides. *Chem. Sci.* **2018**, *9* (45), 8542−8552.
(24) Hossain, A.; Bhattacharyya, A.; Reiser, O. Copper's Rapid Ascent in Visible-Light Photoredox Catalysis. *Science* **2019**, *364* (6439), 9713.
(25) Büldt, L. A.; Wenger, O. S. Chromium Complexes for Luminescence, Solar Cells, Photoredox Catalysis, Upconversion, and Phototriggered NO Release. *Chem. Sci.* **2017**, *8* (11), 7359−7367.
(26) Stevenson, S. M.; Shores, M. P.; Ferreira, E. M. Photooxidizing Chromium Catalysts for Promoting Radical Cation Cycloadditions. *Angew. Chem., Int. Ed.* **2015**, *54* (22), 6506−6510.
(27) Sarabia, F. J.; Ferreira, E. M. Radical Cation Cyclopropanations via Chromium Photooxidative Catalysis. *Org. Lett.* **2017**, *19* (11), 2865−2868.
(28) Sarabia, F. J.; Li, Q.; Ferreira, E. M. Cyclopentene Annulations of Alkene Radical Cations with Vinyl Diazo Species Using Photocatalysis. *Angew. Chem., Int. Ed.* **2018**, *57* (34), 11015−11019.
(29) Treiling, S.; Wang, C.; Förster, C.; Reichenauer, F.; Kalmbach, J.; Boden, P.; Harris, J. P.; Carrella, L. M.; Rentschler, E.; Resch-Genger, U.; Reber, C.; Seitz, M.; Gerhards, M.; Heinze, K. Luminescence and Light-Driven Energy and Electron Transfer from an Exceptionally Long-Lived Excited State of a Non-Innocent Chromium(III) Complex. *Angew. Chem., Int. Ed.* **2019**, *58* (50), 18075−18085.
(30) Tanabe, Y.; Sugano, S. On the Absorption Spectra of Complex Ions. I. *J. Phys. Soc. Jpn.* **1954**, *9* (5), 753−766.
(31) Forster, L. S. Thermal Relaxation in Excited Electronic States of d^3 and d^6 Metal Complexes. *Coord. Chem. Rev.* **2002**, *227* (1), 59−92.
(32) Sinha, N.; Jiménez, J.-R.; Pfund, B.; Prescimone, A.; Piguet, C.; Wenger, O. S. A Near-infrared-II Emissive Chromium(III) Complex. *Angew. Chem., Int. Ed.* **2021**, *60*, 23722−23728, DOI: 10.1002/anie.202106398.
(33) Stein, L.; Boden, P.; Naumann, R.; Förster, C.; Niedner-Schatteburg, G.; Heinze, K. The Overlooked NIR Luminescence of $Cr(ppy)_3$. *Chem. Commun.* **2022**, *58*, 3701.
(34) Schröder, D.; Shaik, S.; Schwarz, H. Two-State Reactivity as a New Concept in Organometallic Chemistry. *Acc. Chem. Res.* **2000**, *33* (3), 139−145.
(35) Shah, S. S.; Maverick, A. W. Photophysics and Photochemistry of 2,2′-Bipyridine and 1,10-Phenanthroline Complexes of Vanadium-(II). *Inorg. Chem.* **1986**, *25* (11), 1867−1871.
(36) Dill, R. D.; Portillo, R. I.; Shepard, S. G.; Shores, M. P.; Rappé, A. K.; Damrauer, N. H. Long-Lived Mixed ^{2}MLCT/MC States in Antiferromagnetically Coupled d^3 Vanadium(II) Bipyridine and Phenanthroline Complexes. *Inorg. Chem.* **2020**, *59* (20), 14706−14715.
(37) Joyce, J. P.; Portillo, R. I.; Nite, C. M.; Nite, J. M.; Nguyen, M. P.; Rappé, A. K.; Shores, M. P. Electronic Structures of Cr(III) and V(II) Polypyridyl Systems: Undertones in an Isoelectronic Analogy. *Inorg. Chem.* **2021**, *60* (17), 12823−12834.
(38) Kirk, A. D. Photochemistry and Photophysics of Chromium-(III) Complexes. *Chem. Rev.* **1999**, *99* (6), 1607−1640, DOI: 10.1021/cr960111+.
(39) Ford, P. C. From Curiosity to Applications. A Personal Perspective on Inorganic Photochemistry. *Chem. Sci.* **2016**, *7* (5), 2964−2986.
(40) Johansson, J. O.; Kim, J.-W.; Allwright, E.; Rogers, D. M.; Robertson, N.; Bigot, J.-Y. Directly Probing Spin Dynamics in a Molecular Magnet with Femtosecond Time-Resolution. *Chem. Sci.* **2016**, *7* (12), 7061−7067.
(41) Zobel, J. P.; González, L. The Quest to Simulate Excited-State Dynamics of Transition Metal Complexes. *JACS Au* **2021**, *1* (8), 1116−1140.
(42) Dorn, M.; Kalmbach, J.; Boden, P.; Päpcke, A.; Gómez, S.; Förster, C.; Kuczelinis, F.; Carrella, L. M.; Büldt, L. A.; Bings, N. H.; Rentschler, E.; Lochbrunner, S.; González, L.; Gerhards, M.; Seitz, M.; Heinze, K. A Vanadium(III) Complex with Blue and NIR-II Spin-Flip Luminescence in Solution. *J. Am. Chem. Soc.* **2020**, *142* (17), 7947−7955.
(43) Dorn, M.; Kalmbach, J.; Boden, P.; Kruse, A.; Dab, C.; Reber, C.; Niedner-Schatteburg, G.; Lochbrunner, S.; Gerhards, M.; Seitz, M.; Heinze, K. Ultrafast and Long-Time Excited State Kinetics of an NIR-Emissive Vanadium(III) Complex I: Synthesis, Spectroscopy and Static Quantum Chemistry. *Chem. Sci.* **2021**, *12*, 10780−10790.
(44) Fataftah, M. S.; Bayliss, S. L.; Laorenza, D. W.; Wang, X.; Phelan, B. T.; Wilson, C. B.; Mintun, P. J.; Kovos, B. D.; Wasielewski, M. R.; Han, S.; Sherwin, M. S.; Awschalom, D. D.; Freedman, D. E. Trigonal Bipyramidal V^{3+} Complex as an Optically Addressable Molecular Qubit Candidate. *J. Am. Chem. Soc.* **2020**, *142* (48), 20400−20408.
(45) Harris, J. P.; Reber, C.; Colmer, H. E.; Jackson, T. A.; Forshaw, A. P.; Smith, J. M.; Kinney, R. A.; Telser, J. Near-Infrared $^2E_g \rightarrow {}^4A_{2g}$ and Visible LMCT Luminescence from a Molecular Bis -(Tris-(Carbene)Borate) Manganese(IV) Complex. *Can. J. Chem.* **2017**, *95* (5), 547−552, DOI: 10.1139/cjc-2016-0607.
(46) Laorenza, D. W.; Kairalapova, A.; Bayliss, S. L.; Goldzak, T.; Greene, S. M.; Weiss, L. R.; Deb, P.; Mintun, P. J.; Collins, K. A.; Awschalom, D. D.; Berkelbach, T. C.; Freedman, D. E. Tunable Cr^{4+} Molecular Color Centers. *J. Am. Chem. Soc.* **2021**, *143* (50), 21350−21363.
(47) Goddard, W. A.; Dunning, T. H.; Hunt, W. J.; Hay, P. J. Generalized Valence Bond Description of Bonding in Low-Lying States of Molecules. *Acc. Chem. Res.* **1973**, *6* (11), 368−376.
(48) Bobrowicz, F. W. *Investigation of Spin-Eigenfunction Correlated Wavefunctions*; California Institute of Technology: Pasadena, CA, 1974.
(49) Bobrowicz, F. W.; Goddard, W. A. The Self-Consistent Field Equations for Generalized Valence Bond and Open-Shell Hartree—Fock Wave Functions. *Methods Electron. Struct. Theory* **1977**, 79−127.
(50) Dunning, T. H.; Xu, L. T.; Cooper, D. L.; Karadakov, P. B. Spin-Coupled Generalized Valence Bond Theory: New Perspectives on the Electronic Structure of Molecules and Chemical Bonds. *J. Phys. Chem. A* **2021**, *125* (10), 2021−2050.
(51) Dunning, T. H.; Xu, L. T.; Takeshita, T. Y.; Lindquist, B. A. Insights into the Electronic Structure of Molecules from Generalized Valence Bond Theory. *J. Phys. Chem. A* **2016**, *120* (11), 1763−1778.
(52) Cooper, D. L.; Gerratt, J.; Raimondi, M. Applications of Spin-Coupled Valence Bond Theory. *Chem. Rev.* **1991**, *91* (5), 929−964.
(53) Dunning, T. H.; Jeffrey Hay, P. Beyond Molecular Orbital Theory: The Impact of Generalized Valence Bond Theory in Molecular Science. *Springer Ser. Mater. Sci.* **2021**, *284*, 55−87.

https://doi.org/10.1021/acs.inorgchem.1c03418
Inorg. Chem. 2022, 61, 6376−6391

(54) Sharma, S.; Andrade, G. A.; Maurya, S.; Popov, I. A.; Batista, E. R.; Davis, B. L.; Mukundan, R.; Smythe, N. C.; Tondreau, A. M.; Yang, P.; Gordon, J. C. Iron-Iminopyridine Complexes as Charge Carriers for Non-Aqueous Redox Flow Battery Applications. *Energy Storage Mater.* **2021**, *37*, 576−586.
(55) Cordero, B.; Gómez, V.; Platero-Prats, A. E.; Revés, M.; Echeverría, J.; Cremades, E.; Barragán, F.; Alvarez, S. Covalent Radii Revisited. *J. Chem. Soc., Dalton Trans.* **2008**, 2832−2838, DOI: 10.1039/B801115J.
(56) Llunell, M.; Casanova, D.; Cierra, J.; Alemany, P. *SHAPE: Program for the Stereochemical Analysis of Molecular Fragments by Means of Continuous Shape Measures and Associated Tools*; Universitat de Barcelona: Barcelona, 2013.
(57) Kirchner, R. M.; Mealli, C.; Bailey, M.; Howe, N.; Torre, L. P.; Wilson, L. J.; Andrews, L. C.; Rose, N. J.; Lingafelter, E. C. The Variable Coordination Chemistry of a Potentially Heptadentate Ligand with a Series of 3d Transition Metal Ions. The Chemistry and Structures of $[M(Py_3tren)]^{2+}$, Where M(II) Mn, Fe, Co, Ni, Cu, and Zn and (Py_3tren) $N\{CH_2CH_2C(H)(C_5H_4N)\}_3$. *Coord. Chem. Rev.* **1987**, *77* (C), 89−163.
(58) Brewer, G. Structural Evidence of Spin State Selection and Spin Crossover Behavior of Tripodal Schiff Base Complexes of Tris(2-Aminoethyl)Amine and Related Tripodal Amines. *Magnetochemistry* **2020**, *6* (2), 28 DOI: 10.3390/magnetochemistry6020028.
(59) Ruiz-Martínez, A.; Casanova, D.; Alvarez, S. Ligand Association/Dissociation Paths and Ill-Defined Coordination Numbers. *Chem. - Eur. J.* **2010**, *16* (22), 6567−6581, DOI: 10.1002/chem.200902996.
(60) Halcrow, M. A. Structure:Function Relationships in Molecular Spin-Crossover Complexes. *Chem. Soc. Rev.* **2011**, *40* (7), 4119−4142.
(61) Alvarez, S. Distortion Pathways of Transition Metal Coordination Polyhedra Induced by Chelating Topology. *Chem. Rev.* **2015**, *115* (24), 13447−13483.
(62) Casanova, D.; Alemany, P.; Bofill, J. M.; Alvarez, S. Shape and Symmetry of Heptacoordinate Transition-Metal Complexes: Structural Trends. *Chem. - Eur. J.* **2003**, *9* (6), 1281−1295, DOI: 10.1002/chem.200390145.
(63) McDaniel, A. M.; Tseng, H. W.; Hill, E. A.; Damrauer, N. H.; Rappé, A. K.; Shores, M. P. Syntheses and Photophysical Investigations of Cr(III) Hexadentate Iminopyridine Complexes and Their Tris(Bidentate) Analogues. *Inorg. Chem.* **2013**, *52* (3), 1368−1378.
(64) Klug, C. M.; Ozumerzifon, T. J.; Bhowmick, I.; Livesay, B. N.; Rappé, A. K.; Shores, M. P. Anionic Guest-Dependent Slow Magnetic Relaxation in Co(II) Tripodal Iminopyridine Complexes. *Dalt. Trans.* **2019**, *48* (25), 9117−9126.
(65) Russo, T. V.; Martin, R. L.; Hay, P. J. Density Functional Calculations on First-Row Transition Metals. *J. Chem. Phys.* **1994**, *101* (9), 7729−7737.
(66) Stratmann, R. E.; Scuseria, G. E.; Frisch, M. J. An Efficient Implementation of Time-Dependent Density-Functional Theory for the Calculation of Excitation Energies of Large Molecules. *J. Chem. Phys.* **1998**, *109* (19), 8218−8224.
(67) Hoffert, W. A.; Rappé, A. K.; Shores, M. P. Topological and Electronic Influences on Magnetic Exchange Coupling in Fe(III) Ethynylbenzene Dendritic Building Blocks. *J. Am. Chem. Soc.* **2011**, *133* (51), 20823−20836.
(68) Konig, E.; Kremer, S. Exact Spin-Pairing Energies at the Crossovers in Octahedral d^4, d^5, d^6, and d^7 Transition Metal Complexes. *Theor. Chim. Acta* **1971**, *23*, 12−20.
(69) Vanquickenborne, L. G.; Haspeslagh, L. On the Meaning of Spin-Pairing Energy in Transition-Metal Ions. *Inorg. Chem.* **1982**, *21* (6), 2448−2454.
(70) Orgel, L. E. Electronic Structures of Transition-Metal Complexes. *J. Chem. Phys.* **1955**, *23* (10), 1819−1823.
(71) Stuyver, T.; Chen, B.; Zeng, T.; Geerlings, P.; De Proft, F.; Hoffmann, R. Do Diradicals Behave like Radicals? *Chem. Rev.* **2019**, *119* (21), 11291−11351.
(72) Dougherty, D. A. Spin Control in Organic Molecules. *Acc. Chem. Res.* **1991**, *24* (3), 88−94.
(73) Borden, W. T.; Davidson, E. R. Effects of Electron Repulsion in Conjugated Hydrocarbon Diradicals. *J. Am. Chem. Soc.* **1977**, *99* (14), 4587−4594.
(74) Shaik, S.; Chen, H.; Janardanan, D. Exchange-Enhanced Reactivity in Bond Activation by Metal-Oxo Enzymes and Synthetic Reagents. *Nat. Chem.* **2011**, *3* (1), 19−27.
(75) Goddard, W. A.; Harding, L. B. The Description of Chemical Bonding From AB Initio Calculations. *Annu. Rev. Phys. Chem.* **1978**, *29* (1), 363−396.
(76) Carter, E. A.; Goddard, W. A. Relationships between Bond Energies in Coordinatively Unsaturated and Coordinatively Saturated Transition-Metal Complexes: A Quantitative Guide for Single, Double, and Triple Bonds. *J. Phys. Chem.* **1988**, *92* (20), 5679−5683.
(77) Jensen, F. *Introduction to Computational Chemistry*, 3rd ed.; John Wiley & Sons: West Sussex, U.K., 2017.
(78) Goldberg, A. H.; Dougherty, D. A. Effects of Through-Bond and through-Space Interactions on Singlet-Triplet Energy Gaps in Localized Biradicals. *J. Am. Chem. Soc.* **1983**, *105* (2), 284−290.
(79) Mecozzi, S.; West, A. P.; Dougherty, D. A. Cation-π Interactions in Aromatics of Biological and Medicinal Interest: Electrostatic Potential Surfaces as a Useful Qualitative Guide. *Proc. Natl. Acad. Sci. U. S. A.* **1996**, *93* (20), 10566−10571.
(80) Sinnecker, S.; Neese, F.; Noodleman, L.; Lubitz, W. Calculating the Electron Paramagnetic Resonance Parameters of Exchange Coupled Transition Metal Complexes Using Broken Symmetry Density Functional Theory: Application to a Mn(III)/Mn(IV) Model Compound. *J. Am. Chem. Soc.* **2004**, *126* (8), 2613−2622, DOI: 10.1021/ja0390202.
(81) Kirchner, B.; Wennmohs, F.; Ye, S.; Neese, F. Theoretical Bioinorganic Chemistry: The Electronic Structure Makes a Difference. *Curr. Opin. Chem. Biol.* **2007**, *11* (2), 134−141.
(82) Roos, B. O.; Taylor, P. R.; Sigbahn, P. E. M. A Complete Active Space SCF Method (CASSCF) Using a Density Matrix Formulated Super-CI Approach. *Chem. Phys.* **1980**, *48* (2), 157−173.
(83) Angeli, C.; Cimiraglia, R.; Evangelisti, S.; Leininger, T.; Malrieu, J. P. Introduction of N-Electron Valence States for Multireference Perturbation Theory. *J. Chem. Phys.* **2001**, *114* (23), 10252.
(84) Angeli, C.; Cimiraglia, R.; Malrieu, J. P. N-Electron Valence State Perturbation Theory: A Fast Implementation of the Strongly Contracted Variant. *Chem. Phys. Lett.* **2001**, *350* (3−4), 297−305.
(85) Angeli, C.; Cimiraglia, R.; Malrieu, J. P. N-Electron Valence State Perturbation Theory: A Spinless Formulation and an Efficient Implementation of the Strongly Contracted and of the Partially Contracted Variants. *J. Chem. Phys.* **2002**, *117* (20), 9138−9153.
(86) Neese, F. Software Update: The ORCA Program System, Version 4.0. *WIREs Comput. Mol. Sci.* **2018**, *8* (1), ZZZ DOI: 10.1002/wcms.1327.
(87) McDaniel, A. M.; Rappé, A. K.; Shores, M. P. Structural and Electronic Comparison of 1st Row Transition Metal Complexes of a Tripodal Iminopyridine Ligand. *Inorg. Chem.* **2012**, *51* (22), 12493−12502.
(88) Deroche, A.; Morgenstern-Badarau, I.; Cesario, M.; Guilhem, J.; Keita, B.; Nadjo, L.; Houée-Levin, C. A Seven-Coordinate Manganese(II) Complex Formed with a Single Tripodal Heptadentate Ligand as a New Superoxide Scavenger. *J. Am. Chem. Soc.* **1996**, *118* (19), 4567−4573.
(89) Pauling, L. The Nature of the Chemical Bond. Application of Results Obtained from the Quantum Mechanics and from a Theory of Paramagnetic Susceptibility to the Structure of Molecules. *J. Am. Chem. Soc.* **1931**, *53* (4), 1367−1400.
(90) Hultgren, R. Equivalent Chemical Bonds Formed by s, p, and d Eigenfunctions. *Phys. Rev.* **1932**, *40* (6), 891−907.
(91) Rappé, A. K.; Goddard, W. A. Titanocyclobutane: Structural Considerations. *J. Am. Chem. Soc.* **1982**, *104* (1), 297−299.
(92) Ozumerzifon, T. J.; Bhowmick, I.; Spaller, W. C.; Rappé, A. K.; Shores, M. P. Toward Steric Control of Guest Binding Modality: A

Cationic Co(II) Complex Exhibiting Cation Binding and Zero-Field Relaxation. *Chem. Commun.* **2017**, *53* (30), 4211−4214.
(93) McGarvey, B. R.; Telser, J. Simple Ligand-Field Theory of d^4 and d^6 Transition Metal Complexes with a C_3 Symmetry Axis. *Inorg. Chem.* **2012**, *51* (11), 6000−6010.
(94) Landis, C. R.; Cleveland, T.; Firman, T. K. Making Sense of the Shapes of Simple Metal Hydrides. *J. Am. Chem. Soc.* **1995**, *117* (6), 1859−1860.
(95) Landis, C. R.; Firman, T. K.; Root, D. M.; Cleveland, T. A Valence Bond Perspective on the Molecular Shapes of Simple Metal Alkyls and Hydrides. *J. Am. Chem. Soc.* **1998**, *120* (8), 1842−1854.
(96) Firman, T. K.; Landis, C. R. Valence Bond Concepts Applied to the Molecular Mechanics Description of Molecular Shapes. 4. Transition Metals with π-Bonds. *J. Am. Chem. Soc.* **2001**, *123* (47), 11728−11742.
(97) Root, D. M.; Landis, C. R.; Cleveland, T. Valence Bond Concepts Applied to the Molecular Mechanics Description of Molecular Shapes. 1. Application to Nonhypervalent Molecules of the P-Block. *J. Am. Chem. Soc.* **1993**, *115* (10), 4201−4209.
(98) Larsen, E.; La Mar, G. N. The Angular Overlap Model: How to Use It and Why. *J. Chem. Educ.* **1974**, *51* (10), 633−640.
(99) Hoffmann, R.; Beier, B. F.; Muetterties, E. L.; Rossi, A. R. Seven-Coordination. A Molecular Orbital Exploration of Structure, Stereochemistry, and Reaction Dynamics. *Inorg. Chem.* **1977**, *16* (3), 511−522.
(100) Kadish, K. M.; Su, C. H.; Schaeper, D.; Merrill, C. L.; Wilson, L. J. Effect of Spin State on the Redox and Electron-Transfer Properties of the Variable-Spin Family of [Fe(II)(6-Mepy)$_n$(Py)$_{3-n}$tren](PF$_6$)$_2$ Complexes in Solution. *Inorg. Chem.* **1982**, *21* (9), 3433−3437.
(101) Ozumerzifon, T. J.; Higgins, R. F.; Joyce, J. P.; Kolanowski, J. L.; Rappé, A. K.; Shores, M. P. Evidence for Reagent-Induced Spin-State Switching in Tripodal Fe(II) Iminopyridine Complexes. *Inorg. Chem.* **2019**, *58* (12), 7785−7793.
(102) Lazar, H. Z.; Forestier, T.; Barrett, S. A.; Kilner, C. A.; Létard, J. F.; Halcrow, M. A. Thermal and Light-Induced Spin-Crossover in Salts of the Heptadentate Complex [tris(4-{pyrazol-3-yl}-3-aza-3-butenyl)amine]Iron(II). *Dalton Trans.* **2007**, No. 38, 4276−4285, DOI: 10.1039/B708971F.
(103) Scarborough, C. C.; Sproules, S.; Doonan, C. J.; Hagen, K. S.; Weyhermüller, T.; Wieghardt, K. Scrutinizing Low-Spin Cr(II) Complexes. *Inorg. Chem.* **2012**, *51* (12), 6969−6982.
(104) Lu, C. C.; Bill, E.; Weyhermüller, T.; Bothe, E.; Wieghardt, K. Neutral Bis(α-Iminopyridine)Metal Complexes of the First-Row Transition Ions (Cr, Mn, Fe, Co, Ni, Zn) and Their Monocationic Analogues: Mixed Valency Involving a Redox Noninnocent Ligand System. *J. Am. Chem. Soc.* **2008**, *130* (10), 3181−3197.
(105) Bowman, A. C.; Sproules, S.; Wieghardt, K. Electronic Structures of the [V(Tbpy)$_3$] z (z = 3+, 2+, 0, 1-) Electron Transfer Series. *Inorg. Chem.* **2012**, *51* (6), 3707−3717.
(106) Sproules, S.; Weyhermüller, T.; Debeer, S.; Wieghardt, K. Six-Membered Electron Transfer Series [V(Dithiolene)$_3$]^z (z = 1+, 0, 1-, 2-, 3-, 4-). An X-Ray Absorption Spectroscopic and Density Functional Theoretical Study. *Inorg. Chem.* **2010**, *49* (11), 5241−5261.
(107) Elliott, N. Magnetic Moments of V^{2+}, Cr^{3+}, and Mn^{4+} Ions in Octahedral Ligand Fields. *J. Chem. Phys.* **2004**, *46* (3), 1006 DOI: 10.1063/1.1840761.
(108) Kahn, O. *Molecular Magnetism*; Wiley-VCH, 1993.
(109) Bendix, J.; Clark, K. M. Delocalization and Valence Tautomerism in Vanadium Tris(Iminosemiquinone) Complexes. *Angew. Chem., Int. Ed.* **2016**, *55* (8), 2748−2752, DOI: 10.1002/anie.201510403.
(110) Clark, K. M.; Bendix, J.; Heyduk, A. F.; Ziller, J. W. Synthesis and Characterization of a Neutral Titanium Tris(Iminosemiquinone) Complex Featuring Redox-Active Ligands. *Inorg. Chem.* **2012**, *51* (14), 7457−7459.
(111) Ghafarian Shirazi, R.; Neese, F.; Pantazis, D. A. Accurate Spin-State Energetics for Aryl Carbenes. *J. Chem. Theory Comput.* **2018**, *14* (9), 4733−4746.
(112) Flöser, B. M.; Guo, Y.; Riplinger, C.; Tuczek, F.; Neese, F. Detailed Pair Natural Orbital-Based Coupled Cluster Studies of Spin Crossover Energetics. *J. Chem. Theory Comput.* **2020**, *16* (4), 2224−2235.
(113) Evans, D. F. 379. Magnetic Perturbation of Singlet−Triplet Transitions. Part V. Mechanism. *J. Chem. Soc.* **1961**, 1987−1993, DOI: 10.1039/JR9610001987.
(114) Anderson, P. W. Antiferromagnetism. Theory of Superexchange Interaction. *Phys. Rev.* **1950**, *79* (2), 350.
(115) Yamashita, J.; Kondo, J. Superexchange Interaction. *Phys. Rev.* **1958**, *109* (3), 730.
(116) Kahn, O.; Briat, B. Exchange Interaction in Polynuclear Complexes. Part 1.—Principles, Model and Application to the Binuclear Complexes of Chromium(III). *J. Chem. Soc. Faraday Trans. 2 Mol. Chem. Phys.* **1976**, *72* (0), 268−281.
(117) Hay, P. J.; Thibeault, J. C.; Hoffmann, R. Orbital Interactions in Metal Dimer Complexes. *J. Am. Chem. Soc.* **1975**, *97* (17), 4884−4899.
(118) Noodleman, L. Valence Bond Description of Antiferromagnetic Coupling in Transition Metal Dimers. *J. Chem. Phys.* **1981**, *74* (10), 5737−5743.
(119) Noodleman, L.; Davidson, E. R. Ligand Spin Polarization and Antiferromagnetic Coupling in Transition Metal Dimers. *Chem. Phys.* **1986**, *109* (1), 131−143.
(120) Neese, F. Definition of Corresponding Orbitals and the Diradical Character in Broken Symmetry DFT Calculations on Spin Coupled Systems. *J. Phys. Chem. Solids* **2004**, *65* (4), 781−785.
(121) Hunt, W. J.; Hay, P. J.; Goddard, W. A., III Self-Consistent Procedures for Generalized Valence Bond Wavefunctions. Applications H_3, BH, H_2O, C_2H_6, and O_2. *J. Chem. Phys.* **1972**, *57* (2), 738 DOI: 10.1063/1.1678308.
(122) Odoh, S. O.; Manni, G. L.; Carlson, R. K.; Truhlar, D. G.; Gagliardi, L. Separated-Pair Approximation and Separated-Pair Pair-Density Functional Theory. *Chem. Sci.* **2016**, *7* (3), 2399−2413.
(123) Thorhallsson, A. T.; Benediktsson, B.; Bjornsson, R. A Model for Dinitrogen Binding in the E_4 State of Nitrogenase. *Chem. Sci.* **2019**, *10* (48), 11110−11124.
(124) Cirera, J.; Via-Nadal, M.; Ruiz, E. Benchmarking Density Functional Methods for Calculation of State Energies of First Row Spin-Crossover Molecules. *Inorg. Chem.* **2018**, *57* (22), 14097−14105.
(125) Shaik, S.; Hiberty, P. C. *A Chemist's Guide to Valence Bond Theory*; John Wiley and Sons, 2007. DOI: 10.1002/9780470192597
(126) Alvarez, S.; Cirera, J. How High the Spin? Allowed and Forbidden Spin States in Transition-Metal Chemistry. *Angew. Chem., Int. Ed.* **2006**, *45* (19), 3012−3020.
(127) Villafañe, F. Dynamic Behavior in Solution of Seven-Coordinated Transition Metal Complexes. *Coord. Chem. Rev.* **2014**, *281*, 86−99.
(128) McDaniel, A. M.; Tseng, H. W.; Damrauer, N. H.; Shores, M. P. Synthesis and Solution Phase Characterization of Strongly Photooxidizing Heteroleptic Cr(III) Tris-Dipyridyl Complexes. *Inorg. Chem.* **2010**, *49* (17), 7981−7991.
(129) Reta, D.; de P. R. Moreira, I.; Illas, F. Magnetic Coupling Constants in Three Electrons Three Centers Problems from Effective Hamiltonian Theory and Validation of Broken Symmetry-Based Approaches. *J. Chem. Theory Comput.* **2016**, *12* (7), 3228−3235, DOI: 10.1021/acs.jctc.6b00413.
(130) Krylov, A. I. Triradicals. *J. Phys. Chem. A* **2005**, *109* (47), 10638−10645.
(131) Winkler, M.; Sander, W. Triradicals. *Acc. Chem. Res.* **2014**, *47* (1), 31−44.
(132) Sugisaki, K.; Toyota, K.; Sato, K.; Shiomi, D.; Takui, T. A Quantum Algorithm for Spin Chemistry: A Bayesian Exchange Coupling Parameter Calculator with Broken-Symmetry Wave Functions. *Chem. Sci.* **2021**, *12* (6), 2121−2132.

https://doi.org/10.1021/acs.inorgchem.1c03418
Inorg. Chem. 2022, 61, 6376−6391

(133) Tichnell, C. R.; Daley, D. R.; Stein, B. W.; Shultz, D. A.; Kirk, M. L.; Danilov, E. O. Wave Function Control of Charge-Separated Excited-State Lifetimes. *J. Am. Chem. Soc.* **2019**, *141* (9), 3986−3992.
(134) Stein, B. W.; Tichnell, C. R.; Chen, J.; Shultz, D. A.; Kirk, M. L. Excited State Magnetic Exchange Interactions Enable Large Spin Polarization Effects. *J. Am. Chem. Soc.* **2018**, *140* (6), 2221−2228.
(135) Bechlars, B.; D'Alessandro, D. M.; Jenkins, D. M.; Iavarone, A. T.; Glover, S. D.; Kubiak, C. P.; Long, J. R. High-Spin Ground States via Electron Delocalization in Mixed-Valence Imidazolate-Bridged Divanadium Complexes. *Nat. Chem.* **2010**, *2* (5), 362−368.
(136) Jäntti, A.; Wagner, M.; Wagner, M.; Suontamo, R.; Kolehmainen, E.; Rissanen, K. Schiff-Base Podates − X-Ray, NMR and Ab Initio Molecular-Orbital Studies of the Cadmium(II) Complexes of Linear and Three-Armed Podands in Solution and Solid State. *Eur. J. Inorg. Chem.* **1998**, *1998* (10), 1555−1562.
(137) Bain, G. A.; Berry, J. F. Diamagnetic Corrections and Pascal's Constants. *J. Chem. Educ.* **2008**, *85* (4), 532−536.
(138) Frisch, M. J.; Trucks, G. W.; Schlegel, H. B.; Scuseria, G. E.; Robb, M. A.; Cheeseman, J. R.; Scalmani, G.; Barone, V.; Petersson, G. A.; Nakatsuji, H.; Li, X.; Caricato, M.; Marenich, A.; Bloino, J.; Janesko, B. G.; Gomperts, R.; Mennucci, B.; Hratchian, H. P.; Ort, J. V.; Fox, D. J. *Gaussian 16*, rev. B.01; Gaussian, Inc.: Wallingford, CT, 2016.
(139) Austin, A.; Petersson, G. A.; Frisch, M. J.; Dobek, F. J.; Scalmani, G.; Throssell, K. A Density Functional with Spherical Atom Dispersion Terms. *J. Chem. Theory Comput.* **2012**, *8* (12), 4989−5007.
(140) Krishnan, R.; Binkley, J. S.; Seeger, R.; Pople, J. A. Self-Consistent Molecular Orbital Methods. XX. A Basis Set for Correlated Wave Functions. *J. Chem. Phys.* **1980**, *72* (1), 650−654.
(141) Tomasi, J.; Mennucci, B.; Cammi, R. Quantum Mechanical Continuum Solvation Models. *Chem. Rev.* **2005**, *105* (8), 2999−3093.
(142) Weigend, F.; Ahlrichs, R. Balanced Basis Sets of Split Valence, Triple Zeta Valence and Quadruple Zeta Valence Quality for H to Rn: Design and Assessment of Accuracy. *Phys. Chem. Chem. Phys.* **2005**, *7* (18), 3297−3305.

https://doi.org/10.1021/acs.inorgchem.1c03418
Inorg. Chem. 2022, 61, 6376−6391